

# Beta-plane turbulence above monoscale topography

Navid C. Constantinou<sup>1</sup>†, and William R. Young<sup>1</sup>

<sup>1</sup>Scripps Institution of Oceanography, University of California San Diego, La Jolla, CA 90293-0213, USA

(Received xx; revised xx; accepted xx)

Wind is an important driver of large-scale ocean currents, imparting momentum into the ocean at the sea surface. This force is almost entirely balanced by topographic form stress (that is the correlation of bottom pressure and topographic slope). The direct effect of bottom or skin friction in turbulent boundary layers is almost negligible for the momentum balance. We use a one-layer quasi-geostrophic model to study the effect of a random monoscale bottom topography on beta-plane geostrophic turbulence. The model forcing is a uniform steady wind stress that produces both a uniform large-scale flow  $U(t)$  and smaller-scale macroturbulence. The macroturbulence is characterized by both standing and transient eddies and the large scale flow  $U$  is retarded by a combination of bottom drag and domain-averaged topographic form stress produced by the standing eddies. A collection of statistically equilibrated numerical solutions delineates the main flow regimes and the dependence of the time-average of  $U$  on parameters such as the planetary vorticity gradient  $\beta$  and the statistical properties of the topography.

A main control parameter is the ratio of  $\beta$  to the root mean square gradient of the topographic potential vorticity (PV). We derive asymptotic scaling laws for the strength of the large-scale flow in the limiting cases of weak and strong forcing. If  $\beta$  is comparable to, or larger than, the topographic PV gradient there is an “eddy saturation” regime in which  $U$  is insensitive to large changes in the wind stress. We show that eddy saturation requires strong transient eddies that act effectively as PV diffusion. This diffusion does not decrease the strength of the standing eddies but it does increase the form stress by enhancing the correlation between topographic slope and the standing eddy pressure field. Using bounds based on the energy and enstrophy power integrals we show that as the strength of the wind stress increases the flow transitions from a regime in which most of the form stress balances the wind stress to a regime in which the form stress is very small and large transport ensues.

**Key words:** Geostrophic turbulence, Quasi-geostrophic flows, Topographic effects

## 1. Introduction

Winds force the oceans by applying a stress at the sea surface. A question of interest is where and how this vertical flux of horizontal momentum into the ocean is balanced. Consider, for example, a steady zonal wind blowing over the sea surface and exerting a force on the ocean. In a statistically steady state we can identify all possible mechanisms for balancing this surface force by first vertically integrating over the depth of the ocean,

† Email address for correspondence: navid@ucsd.edu

Table 1: Various idealized topographies  $h(x, y)$  previously used in the literature.

Charney & DeVore (1979)	$\cos(m\pi x) \sin(n\pi y)$
Charney <i>et al.</i> (1981)	$f(x) \sin(\pi y)$
Hart (1979)	$\cos(2\pi x)$ (& remarks on $f(y) \cos(2\pi x)$ )
Davey (1980)	triangular ridge: $f(x) \sin(\pi y)$
Pedlosky (1981)	$\cos(m\pi x) \sin(n\pi y)$
Källén (1982)	$P_3^2(r) \cos(3\phi)$ (on the sphere)
Legras & Ghil (1985)	$P_2^1(r) \cos(2\phi)$ (on the sphere)
Rambaldi & Flierl (1984)	$\sin(2\pi x)$
Rambaldi & Mo (1984)	$\sin(\pi y) \sin(4\pi x)$
Yoden (1985)	$\cos(m\pi x) \sin(n\pi y)$
Tung & Rosenthal (1985)	$\cos(m\pi x) \sin(n\pi y)$

and then horizontally integrating over a region in which the wind stress is approximately uniform. Following the strategy of Bretherton & Karweit (1975), we have in mind a mid-ocean region which is much smaller than ocean basins, but much larger than the length scale of ocean macroturbulence. The zonal wind stress on this volume can be balanced by several processes which we classify as either local or non-local. The most obvious local process is skin friction in turbulent bottom boundary layers. But in the deep ocean skin friction is negligible (Munk & Palmén 1951); instead the most important local process is topographic form stress (the correlation of pressure and topographic slope). Topographic form stress is an inviscid mechanism for coupling the ocean to the solid Earth. Non-local processes include the advection of zonal momentum out of the domain and, most importantly, the possibility that a large-scale pressure gradient is supported by piling water up against either distant continental boundaries or ridge systems.

In this paper we concentrate on the local processes that balance wind stress and result in homogeneous ocean macroturbulence. Thus we investigate the simplest model of topographic form stress defined in (2.4) and (2.6) below. This is a single-layer quasi-geostrophic model, forced by a steady zonal mean wind stress in a doubly periodic domain. A distinctive feature of the model is the uniform large-scale zonal flow  $U(t)$  in (2.6) that is accelerated by an applied uniform wind stress and resisted by skin friction and domain-averaged topographic form stress (Hart 1979; Davey 1980; Holloway 1987; Carnevale & Frederiksen 1987). By construction we exclude the possibility of a large-scale non-local pressure gradient.

This model, without a non-local pressure gradient, may be particularly pertinent to the Southern Ocean. There, the absence of continental boundaries along a range of latitudes implies that a large-scale pressure gradient cannot be invoked in balancing the zonal wind stress. However, we emphasize that the model in (2.4) and (2.6) may also be relevant in a small region of the ocean away from any continental boundaries, where we expect a statistically homogeneous eddy field. Although the model has been derived previously by several authors, it has never been investigated in detail except for the simplest model topographies summarized in table 1. Here, we delineate the various flow regimes of geostrophic turbulence above a homogeneous, isotropic and monoscale topography (see figure 1).

Very similar models were developed in meteorology in order to understand stationary waves and blocking patterns. Charney & DeVore (1979) introduced a reduced model of the interaction of zonal flow and topography and, within this model, they demonstrated the possibility of multiple equilibrium states, one of which corresponds to a blocked state. Charney & DeVore (1979) paved the way for a series of studies directed at understanding the existence of multiple stable solutions to systems such as (2.4) and (2.6) (Charney *et al.* 1981; Hart 1979; Davey 1980; Pedlosky 1981; Källén 1982; Rambaldi & Flierl 1984; Rambaldi & Mo 1984; Yoden 1985; Tung & Rosenthal 1985; Legras & Ghil 1985). The meteorological literature is mainly concerned with planetary-scale topography e.g., note the use of low-order spherical harmonics and small wavenumbers in table 1. Reflecting our interest in oceanographic issues, here we consider smaller scale topography such as features with 10 to 100 km scale i.e., topography with roughly the same scale as ocean macroturbulence. Despite this difference, we also find a regime in which the model has multiple stable solutions and hysteresis (section 4).

In the context of geostrophic turbulence above small-scale topography there have been two main theoretical approaches: (*i*) statistical and turbulence-closure theories and (*ii*) equilibrium statistical mechanics. Approach (*i*) constructs evolution equations for the vorticity spectrum and the vorticity-topography cross-spectrum and solving for the stationary statistics (Herring 1977; Holloway 1987; Zou & Holloway 1993; Venaille 2012). Approach (*ii*) refers to predictions of the energy or enstrophy spectrum using equilibrium statistical mechanics and the maximum entropy principle (Salmon *et al.* 1976; Carnevale & Frederiksen 1987). Equilibrium statistical mechanics applies directly only to inviscid and unforced flows. Another approach is the minimum enstrophy principle of Bretherton & Haidvogel (1976) which applies mainly to the initial value problem. These strategies are not easily adapted to the forced and dissipative problem studied here. Indeed, we find that some of the main predictions (e.g., a negative correlation between vorticity and topography) are not always in agreement with numerical solution of (2.4) and (2.6) (sections 3 and 4).

Recently, the problem of large-scale ocean flow above topography has attracted further attention because of its implications for the global climate. Observations suggest that the strength of the westerly winds that force the Southern Ocean are increasing (Marshall 2003; Swart & Fyfe 2012). How will the Southern Ocean respond to an increase in wind stress? Is there a linear relationship between wind stress and large-scale zonal transport? There is compelling evidence that in the Southern Ocean the zonal mass transport of the Antarctic Circumpolar Current (ACC) is insensitive to changes in the strength of wind stress forcing. This so-called “eddy saturation” has been documented in numerical simulations (Farneti *et al.* 2015) and there are also indications of eddy saturation in observations of the Southern Ocean (Böning *et al.* 2008; Firing *et al.* 2011; Hogg *et al.* 2015). Straub (1993) predicted that the ACC transport should become insensitive to the wind stress forcing at sufficiently high stress. However, Straub’s argument invoked baroclinicity and channel walls as crucial ingredients for eddy saturation. We are surprised here to discover that a single-layer fluid in a doubly periodic geometry exhibits impressive eddy saturation in certain parameter regimes (section 8).

A main result of this paper is the control of form stress and large-scale transport by a competition between the planetary vorticity gradient  $\beta$  and the r.m.s. gradient of the topographic potential vorticity. We derive asymptotic scaling laws for the dependence of large-scale flow on the strength of the forcing (sections 6 and 7). We provide an explanation for the eddy saturation regime that this model exhibits in certain parameter ranges (section 8.1). Last, we show using the energy and enstrophy power integrals that as the strength of the wind stress increases the flow transitions from a regime in which

the form stress balances almost all of the wind stress to a state in which the form stress vanishes and a very large transport ensues (section 8.2).

## 2. Formulation

We consider barotropic beta-plane flow with the fluid velocity consisting of a large-scale zonal flow,  $U(t)$ , along the axis of  $x$  plus smaller scale eddies with velocity  $(u, v)$ ; thus the total flow is

$$\mathbf{U} \stackrel{\text{def}}{=} (U(t) + u(x, y, t), v(x, y, t)). \quad (2.1)$$

The eddying component of the flow is derived from an eddy streamfunction  $\psi(x, y, t)$  via  $(u, v) = (-\psi_y, \psi_x)$ ; the total streamfunction is  $-U(t)y + \psi(x, y, t)$ . The relative vorticity is

$$\zeta \stackrel{\text{def}}{=} \nabla^2 \psi, \quad (2.2)$$

where  $\nabla^2 \stackrel{\text{def}}{=} \partial_x^2 + \partial_y^2$  and the quasi-geostrophic potential vorticity (QGPV) of the flow is

$$\beta y + \underbrace{\zeta + \eta}_{\stackrel{\text{def}}{=} q}. \quad (2.3)$$

In (2.3),  $\beta$  is the meridional planetary vorticity gradient and  $\eta(x, y)$  is the topographic contribution to potential vorticity. Specifically, if the depth of the fluid is  $H - h(x, y)$ , where  $h(x, y)/H$  is order Rossby number, then  $\eta(x, y) = f_0 h(x, y)/H$  with  $f_0$  the Coriolis parameter in the center of the domain. We refer to  $\eta$  as the *topographic PV*.

The QGPV equation is:

$$q_t + J(\psi - Uy, q + \beta y) + D\zeta = 0, \quad (2.4)$$

where  $J$  is the Jacobian,  $J(a, b) \stackrel{\text{def}}{=} a_x b_y - a_y b_x$ . With Navier–Stokes viscosity  $\nu$  and linear Ekman drag  $\mu$  the “dissipation operator”  $D$  in (2.4) is

$$D \stackrel{\text{def}}{=} \mu - \nu \nabla^2. \quad (2.5)$$

The domain is periodic in both the zonal and meridional direction, with size  $2\pi L \times 2\pi L$ . In numerical solutions, instead of Navier–Stokes viscosity  $\nu \nabla^2$  in (2.5), we use either hyperviscosity  $\nu_4 \nabla^8$ , or a high-wavenumber filter. Thus we achieve a regime in which the role of lateral dissipation is limited to removal small-scale vorticity: the lateral dissipation has a very small effect on larger scales and energy dissipation is mainly due to drag  $\mu$ .

The large-scale flow  $U(t)$  evolves via the domain-averaged zonal momentum equation

$$U_t = F - \mu U - \langle \psi \eta_x \rangle, \quad (2.6)$$

(Hart 1979; Davey 1980; Holloway 1987; Carnevale & Frederiksen 1987). On the right of (2.6),  $\langle \psi \eta_x \rangle$  is the form stress, with angle brackets denoting an average over the  $(x, y)$ -domain. The large-scale flow is forced by the constant  $F = \tau/(\rho_0 H)$ , where  $\tau$  is the uniform surface wind stress and  $\rho_0$  is the reference density of the fluid.

The model formulated above in (2.4) and (2.6) is the simplest process model which can be used to investigate homogeneous beta-plane turbulence driven by a large-scale wind stress applied at the surface of the fluid.

Although the forcing  $F$  in (2.6) is steady, the solution often is not: with strong forcing the flow spontaneously develops time-varying eddies. In those cases it is useful to decompose the eddy streamfunction  $\psi$  into time-mean “standing eddies”, with streamfunction  $\bar{\psi}$ , and

residual “transient eddies”  $\psi'$ :

$$\psi(x, y, t) = \bar{\psi}(x, y) + \psi'(x, y, t), \quad (2.7)$$

where the time-mean is

$$\bar{\psi}(x, y) \stackrel{\text{def}}{=} \lim_{T \rightarrow \infty} \frac{1}{T} \int_{t_1}^{t_1+T} \psi(x, y, t') dt'. \quad (2.8)$$

Using the time average (2.8), all fields can then be decomposed into time-mean and transient components e.g.,  $U(t) = \bar{U} + U'(t)$ . A main question is how  $\bar{U}$  depends on  $F$ ,  $\mu$ ,  $\beta$  as well as the statistical and geometrical properties of the topographic PV  $\eta$ .

### 2.1. Energy and enstrophy power integrals

The energy and enstrophy of the flow are:

$$E \stackrel{\text{def}}{=} \underbrace{\frac{1}{2} U^2}_{\stackrel{\text{def}}{=} E_U} + \underbrace{\frac{1}{2} \langle |\nabla \psi|^2 \rangle}_{\stackrel{\text{def}}{=} E_\psi}, \quad (2.9a)$$

$$Q \stackrel{\text{def}}{=} \underbrace{\beta U}_{\stackrel{\text{def}}{=} Q_U} + \underbrace{\frac{1}{2} \langle q^2 \rangle}_{\stackrel{\text{def}}{=} Q_\psi}. \quad (2.9b)$$

From (2.4) and (2.6) we find that:

$$\frac{dE}{dt} = FU - \mu U^2 - \langle \mu |\nabla \psi|^2 + \nu \zeta^2 \rangle, \quad (2.10a)$$

$$\frac{dQ}{dt} = F\beta - \langle \eta D\zeta \rangle - \mu \beta U - \langle \mu \zeta^2 + \nu |\nabla \zeta|^2 \rangle. \quad (2.10b)$$

The rate of working by the wind stress,  $FU$ , appears on the right of (2.10a): because  $F$  is constant the energy injection varies directly with the large-scale mean flow  $U(t)$ . On the other hand, the main enstrophy injection rate on the right of (2.10b) is fixed and equal to  $F\beta$ . Bretherton & Haidvogel (1976) noted that the term  $\langle \eta D\zeta \rangle$  in (2.10b) is not necessarily positive and might therefore result in enstrophy injection, in addition to the main source  $F\beta$ . The subsidiary enstrophy source  $\langle \eta D\zeta \rangle$  becomes important if  $\beta$  is small relative to the gradients of the topographic PV; in the special case  $\beta = 0$ ,  $\langle \eta D\zeta \rangle$  is the only enstrophy source.

Appendix A provides a detailed discussion of the energy and enstrophy balances. The total energy balance of the eddy field is given as the sum of (A 4c) and (A 4d):

$$\overline{U \langle \psi \eta_x \rangle} = \overline{\langle \mu |\nabla \psi|^2 + \nu \zeta^2 \rangle}. \quad (2.11)$$

The right hand side of (2.11) is positive definite and thus  $U(t)$  is positively correlated with the form stress  $\langle \psi \eta_x \rangle$ . In this sense, the form stress is necessarily acting as increased frictional drag on the large-scale mean flow  $U$ .

If the QGPV equation (2.4) contained additional “eddy forcing” that injected eddy energy at rate  $\varepsilon$  (perhaps due to eddy-scale wind stress curl) then (2.11) would read:  $\overline{U \langle \psi \eta_x \rangle} = \overline{\langle \mu |\nabla \psi|^2 + \nu \zeta^2 \rangle} - \varepsilon$ . With this modification the form stress might be anti-correlated with  $U$ , thus acting in an “anti-frictional” sense to reinforce the large-scale flow  $U$ . Holloway (1992) refers to this anti-friction as the “Neptune effect”. Our decision not to include direct eddy forcing in the QGPV equation implies that the Neptune effect is inoperative.

## 2.2. The sign of $F$ and a QG symmetry broken by $\beta$

We focus exclusively on the case  $F > 0$  i.e., the prevailing mid-latitude case of an eastward wind stress. If and only if  $\beta = 0$  one can use a symmetry of the QG equations to convert the  $F < 0$  problem into an equivalent problem with  $F > 0$ . Suppose  $F < 0$  and define new variables

$$\tilde{U} = -U, \quad (\tilde{x}, \tilde{y}) = -(x, y), \quad (\tilde{\psi}, \tilde{\eta}) = (\psi, \eta). \quad (2.12)$$

In terms of the “tilde variables” the large scale momentum equation (2.6) is

$$\tilde{U}_t = |F| - \mu \tilde{U} - \langle \tilde{\psi} \tilde{\eta}_{\tilde{x}} \rangle. \quad (2.13)$$

Thus the change of variables has reversed the sign of the forcing. On the other hand, using the tilde variables, the QGPV equation (2.4) becomes

$$\tilde{q}_t + \tilde{\mathbf{J}}(\tilde{\psi} - U\tilde{y}, \tilde{q} - \beta\tilde{y}) + \tilde{\mathbf{D}}\tilde{\zeta} = 0. \quad (2.14)$$

The sign of  $\beta$  in (2.14) is reversed relative to that in (2.4). Provided that  $\beta = 0$  this change of variables converts the problem with  $F < 0$  into an equivalent tilde problem with  $F > 0$ . However, non-zero  $\beta$  breaks this symmetry so that the problem with  $F < 0$  is different from that with  $F > 0$ . This symmetry breaking is a result of Rossby wave propagation and the form stress associated with wave drag: if  $U > 0$  then radiation of stationary Rossby lee waves is a potent mechanism resulting in form stress. However, for  $U < 0$  i.e., when the flow is forced by a westward wind stress, topographically excited Rossby waves cannot be stationary and thus wave drag on the large-scale is absent. This was first noted by Bretherton & Karweit (1975) (see also discussions by Davey (1980); Haidvogel & Brink (1986)). This asymmetry is the reason why Haidvogel & Brink (1986) find mean currents using an oscillatory wind stress forcing with zero mean.

## 3. Parameter values and illustrative solutions

Although the barotropic quasi-geostrophic model summarized in section 2 is idealized, it is instructive to estimate  $U$  using numbers loosely inspired by the dynamics of the Southern Ocean: see table 2. Without form stress, the equilibrated large-scale velocity obtained from the large-scale momentum equation (2.6) using  $F$  from table 2 is

$$\frac{F}{\mu} = 0.77 \text{ m s}^{-1}. \quad (3.1)$$

The main point of Munk & Palmén (1951) is that this drag-balanced large-scale velocity is far too large. For example, the implied transport through a meridional section 1000 km long is over 3000 Sverdrups; this is larger by a factor of about twenty than the observed transport of the Antarctic Circumpolar Current (see for example Koenig *et al.* (2016); Donohue *et al.* (2016)).

### 3.1. The topography and geostrophic contours

If the topographic height has a root mean square value of order 200 m, typical of abyssal hills (Goff 2010), then  $\eta_{\text{rms}}^{-1}$  is less than 2 days. Thus even rather small topographic features produce a topographic PV with a time scale that is much less than that of the typical drag coefficient in table 2. This order of magnitude estimate indicates that the form stress is likely to be large. To say more about form stress we must introduce the model topography with more detail.

Table 2: Numerical values characteristic of the Southern Ocean;  $f_0 = -1.26 \times 10^{-4} \text{ s}^{-1}$  and  $\beta = 1.14 \times 10^{-11} \text{ m}^{-1}\text{s}^{-1}$ . The drag coefficient  $\mu$  is taken from [Arbic & Flierl \(2004\)](#).

domain size, $2\pi L \times 2\pi L$	$L$	800 km
mean depth	$H$	4000 m
density of seawater	$\rho_0$	$1035 \text{ kg m}^{-3}$
r.m.s. topographic height	$h_{\text{rms}}$	200 m
r.m.s. topographic PV	$\eta_{\text{rms}} = f_0 h_{\text{rms}} / H$	$6.30 \times 10^{-6} \text{ s}^{-1}$
drag coefficient	$\mu$	$6.30 \times 10^{-8} \text{ s}^{-1}$
wind stress	$\tau$	$0.20 \text{ N m}^{-2}$
forcing on the right of (2.6)	$F = \tau / (\rho_0 H)$	$4.83 \times 10^{-8} \text{ m s}^{-2}$
topographic length scale	$\ell_\eta = 0.0690L$	55.20 km
r.m.s. topographic slope	$h_{\text{rms}} / \ell_\eta$	$3.62 \times 10^{-3}$
a velocity scale	$\beta \ell_\eta^2$	$3.47 \times 10^{-2} \text{ m s}^{-1}$
non-dimensional $\beta$	$\beta \ell_\eta / \eta_{\text{rms}}$	$1.00 \times 10^{-1}$
non-dimensional drag	$\mu / \eta_{\text{rms}}$	$1.00 \times 10^{-2}$
non-dimensional forcing	$F / (\mu \eta_{\text{rms}} \ell_\eta)$	2.20

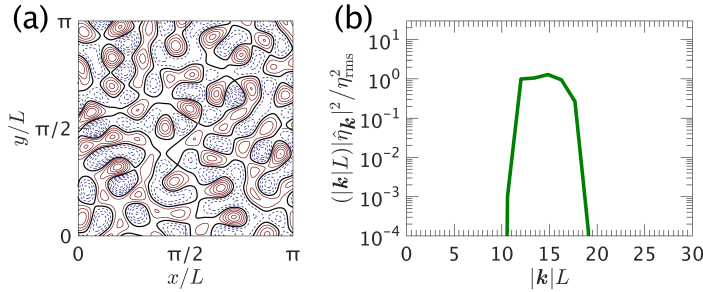


Figure 1: The structure and spectrum of the topography used in this study. Panel (a) shows the structure of the topography for a quarter of the full domain. Solid curves are positive contours, dashed curves negative contours and the thick curves marks the zero contour. Panel (b) shows the 1D power spectrum. The topography has power only within the annulus  $12 \leq |\mathbf{k}|L \leq 18$ .

The topography is synthesized as

$$\eta(x, y) = \sum_{\mathbf{k}} e^{i\mathbf{k} \cdot \mathbf{x}} \eta_{\mathbf{k}}, \quad (3.2)$$

with random phases for  $\eta_{\mathbf{k}}$ . We consider a homogeneous and isotropic topographic model illustrated in figure 1. The topography is constructed by confining the wavenumbers in (3.2) to a relatively narrow annulus with  $12 \leq |\mathbf{k}|L \leq 18$ . The spectral cut-off is tapered smoothly to zero at the edge of the annulus. In addition to being homogeneous and isotropic, the topographic model in figure 1 is approximately *monoscale* i.e., the topography is characterized by a single length scale determined, for instance, by the

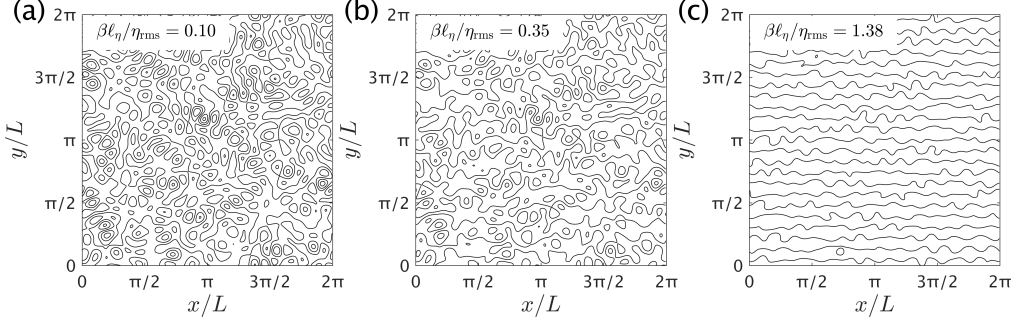


Figure 2: The structure of the geostrophic contours,  $\beta y + \eta$ , for the monoscale topography of figure 1 and for various values of (a)  $\beta\ell_\eta/\eta_{\text{rms}} = 0.10$ , (b)  $\beta\ell_\eta/\eta_{\text{rms}} = 0.35$  and (c)  $\beta\ell_\eta/\eta_{\text{rms}} = 1.38$ . It is difficult to visually distinguish the geostrophic contours with  $\beta\ell_\eta/\eta_{\text{rms}} = 0$  from those with  $\beta\ell_\eta/\eta_{\text{rms}} = 0.1$  in panel (a).

central wavenumber  $|\mathbf{k}| \approx 15/L$  in figure 1(b). To assess the validity of the monoscale approximation we characterize the topography using the length scales

$$\ell_\eta \stackrel{\text{def}}{=} \sqrt{\sum_{\mathbf{k}} |\eta_{\mathbf{k}}|^2 / \sum_{\mathbf{k}} |\mathbf{k}|^2 |\eta_{\mathbf{k}}|^2} = \sqrt{\langle \eta^2 \rangle / \langle |\nabla \eta|^2 \rangle}, \quad (3.3a)$$

and

$$L_\eta \stackrel{\text{def}}{=} \sqrt{\sum_{\mathbf{k}} |\mathbf{k}|^{-2} |\eta_{\mathbf{k}}|^2 / \sum_{\mathbf{k}} |\eta_{\mathbf{k}}|^2} = \sqrt{\langle |\nabla \nabla^{-2} \eta|^2 \rangle / \langle \eta^2 \rangle}. \quad (3.3b)$$

For the model in figure 1

$$\ell_\eta = 0.0690 L \quad \text{and} \quad L_\eta = 0.0707 L. \quad (3.4)$$

(Recall the domain is  $2\pi L \times 2\pi L$ .) Because  $\ell_\eta \approx L_\eta$  we conclude that the topography in figure 1 is monoscale to a good approximation and we use the slope-based length  $\ell_\eta$  as the typical length scale of the topography.

The isotropic homogeneous monoscale model adopted here has no claims to realism. However, the monoscale assumption greatly simplifies many aspects of the problem because all relevant second-order statistical characteristics of the model topography can be expressed in terms of the two dimensional quantities  $\eta_{\text{rms}}$  and  $\ell_\eta$  e.g.,  $\langle (\nabla^{-2} \eta_x)^2 \rangle = \frac{1}{2} \ell_\eta^2 \eta_{\text{rms}}^2$ . The main advantage of monoscale topography is that despite the simplicity of its spectral characterization it exhibits the crucial distinction between open and closed *geostrophic contours*: see figure 2.

The environmental PV is the field  $\beta y + \eta$  and we refer to contours of constant  $\beta y + \eta$  as geostrophic contours. Closed geostrophic contours enclose isolated pools within the domain — see figure 2(a) — while open contours thread through the domain, connecting one side to the other — see figure 2(c). The transition between the two limiting cases is controlled by the ratio of the planetary vorticity gradient over the r.m.s. of the topographic PV gradient,  $\beta\ell_\eta/\eta_{\text{rms}}$ . Figure 2(b) shows an intermediate case with a mixture of closed and open geostrophic contours.

It is instructive to consider the extreme case  $\beta = 0$ . Then only the geostrophic contour  $\eta = 0$  is open and all other geostrophic contours are closed. This intuitive conclusion relies on a special property of the random topography in figure 1: the topography  $-\eta$  is

statistically equivalent  $+\eta$ . In other words, if  $\eta(x, y)$  is in the ensemble then so is  $-\eta(x, y)$ . For further discussion of this conclusion see the discussion of continuum percolation by Efros (1987) and Isichenko (1992).

If  $\beta$  is non-zero, but small in the sense that  $\beta \ll \eta_{\text{rms}}/\ell_\eta$ , then most of the domain is within closed contours: see figure 2(a). In this case, the planetary PV gradient  $\beta$  is too small relative to  $\nabla\eta$  to destroy local pools of closed geostrophic contours. But  $\beta$  dominates the long-range structure of the environmental PV and opens up narrow, meandering domain-spanning channels (Isichenko 1992).

The other extreme is  $\beta\ell_\eta/\eta_{\text{rms}} \gg 1$ ; in this case, illustrated in figure 2(c), all geostrophic contours are open. Because of its geometric simplicity the situation with  $\beta\ell_\eta/\eta_{\text{rms}} \gg 1$  is the easiest to analyze and understand. Unfortunately the difficult case in figure 2(a) is most relevant to ocean conditions. In sections 3.2 and 3.3 we illustrate the two cases using numerical solutions of (2.4) and (2.6).

### 3.2. An example with mostly closed geostrophic contours: $\beta\ell_\eta/\eta_{\text{rms}} = 0.1$

Figures 3 and 4 show a numerical solution for a case with mostly closed geostrophic contours. In this illustration we use the Southern-ocean parameter values in table 2. The solution employs  $1024 \times 1024$  grid points with a high wavenumber filter that removes vorticity at small scales. The system is evolved using the ETDRK4 time-stepping scheme of Cox & Matthews (2002) with the refinement of Kassam & Trefethen (2005).

Figure 3(a) shows the evolution of the large scale flow  $U(t)$  and the form stress  $\langle \psi \eta_x \rangle$ . After a spin-up of duration  $\sim \mu^{-1}$  the flow achieves a statistically steady state in which  $U(t)$  fluctuates around the time mean  $\bar{U}$ . In figure 3(a) the form stress  $\langle \bar{\psi} \eta_x \rangle$  balances almost 98%  $F$ , so that  $U(t)$  is very much smaller than  $F/\mu$  in (3.1). The time-mean of the large scale flow is

$$\bar{U} = 1.70 \text{ cm s}^{-1}, \quad (3.5)$$

which is 2.2% of the velocity  $F/\mu$  in (3.1). Figure 3(b) shows the evolution of the energy: the eddy energy  $E_\psi = \frac{1}{2}\langle |\nabla\psi|^2 \rangle$  is about 50 times greater than the large-scale energy  $E_U = \frac{1}{2}U^2$ . With the decomposition of  $\psi$  in (2.7) the time-mean eddy energy  $\bar{E}_\psi$  is decomposed into  $\bar{E}_{\bar{\psi}} + \overline{E_\psi}$ ; the dash-dot line in figure 3(b) is the energy of the standing component  $\bar{E}_{\bar{\psi}}$ : the transient eddies are less energetic than the standing eddies. This is also evident by comparing the snapshot of  $\zeta$  in figure 4(c) with the time mean  $\bar{\zeta}$  in figure 4(d).

In agreement with the conclusion of Bretherton & Haidvogel (1976), figures 3(c) and (d) show that there is anti-correlation between the relative vorticity and the topographic PV. For the mean  $\bar{\zeta}$ :

$$\langle \bar{\zeta} \eta \rangle / \sqrt{\langle \bar{\zeta}^2 \rangle \langle \eta^2 \rangle} = -0.53. \quad (3.6)$$

Another statistical characterization of the solution is that

$$\langle \bar{\psi} \eta_x \rangle / \sqrt{\langle \bar{\psi}^2 \rangle \langle \eta_x^2 \rangle} = 0.06. \quad (3.7)$$

Thus a rather weak correlation between the standing streamfunction  $\bar{\psi}$  and the topographic PV gradient  $\eta_x$  is sufficient to produce a form stress balancing about 98% the applied wind stress.

The most striking characterization of the time-mean flow is that it is very weak in most of the domain: figure 4(a) shows that most of the flow through the domain is channeled into a relatively narrow band centered very roughly on  $y/L = \pi/2$ : this “main channel” coincides with the extreme values of  $\zeta$  and  $\bar{\zeta}$  evident in figures 3(c) and (d). Outside

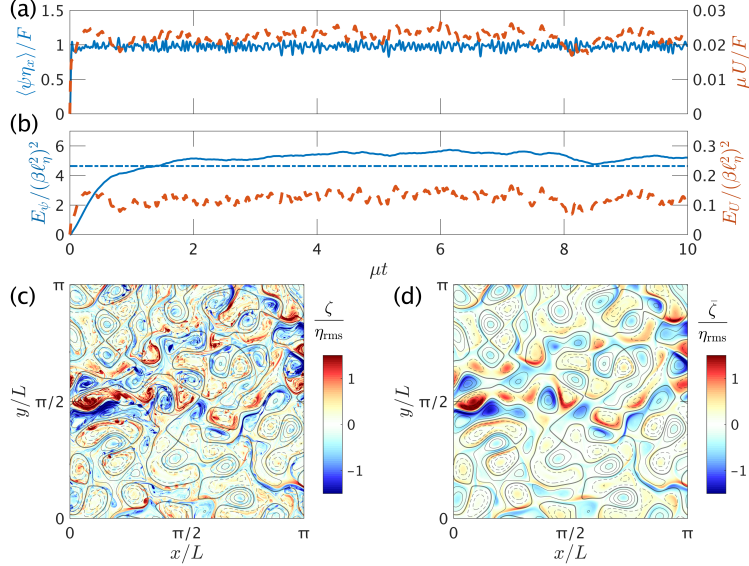


Figure 3: A solution with  $\beta \ell_\eta / \eta_{\text{rms}} = 0.1$  and  $F / (\mu \eta_{\text{rms}} \ell_\eta) = 2.20$ . Panel (a) shows the evolution of the large-scale flow  $U(t)$  (dashed) and the form stress  $\langle \psi \eta_x \rangle$  (solid). Panel (b) shows the evolution of  $E_\psi$  (solid) and  $E_U$  (dashed). The dash-dot line in panel (b) is the energy level of the standing eddies,  $\frac{1}{2} |\nabla \bar{\psi}|^2$ . Panel (c) shows a snapshot of the relative vorticity,  $\zeta$ , (shaded) at  $\mu t = 10$  in one-quarter of the domain overlying the topographic PV (solid contours are positive  $\eta$  and dashed contours are negative). Panel (d) shows the time-mean  $\bar{\zeta}$ . A movie showing the evolution of  $\zeta$  and  $\psi$  from rest is in **Supplementary Materials**.

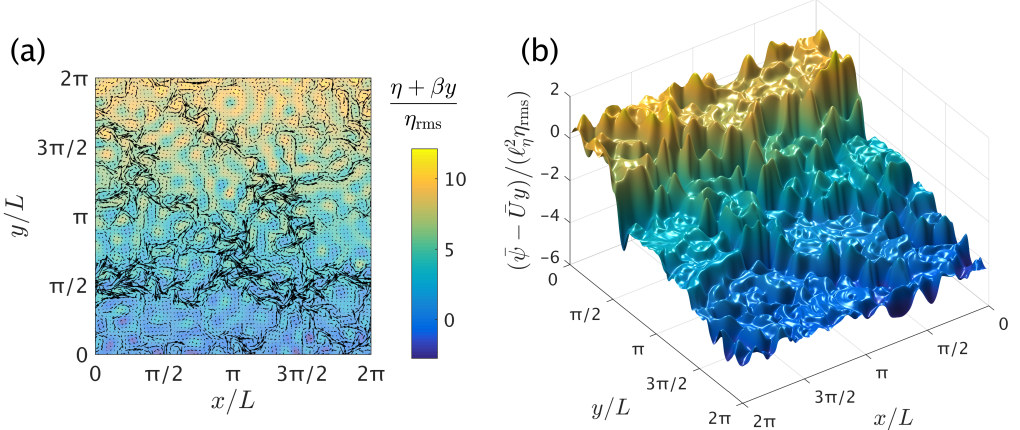


Figure 4: A solution with  $\beta \ell_\eta / \eta_{\text{rms}} = 0.1$  and  $F / (\mu \eta_{\text{rms}} \ell_\eta) = 2.20$ . (a) The environmental PV,  $\eta + \beta y$ , (shaded) and the time-mean velocity field,  $\bar{\mathbf{U}}$ , as arrows. (b) Surface plot of the total time-mean streamfunction,  $\bar{\psi} - \bar{U}y$ .

of the main channel the time-mean flow is weak. We emphasize that  $\bar{U}$  in (3.5) is an unoccupied mean that is not representative of the larger velocities in the main channel: these are 40 to 50 times  $\bar{U}$ .

Figure 4(b) shows the streamfunction  $\bar{\psi}(x, y) - \bar{U}y$  as a surface above the  $(x, y)$ -plane.

The mean streamfunction surface appears as a terraced hillside: the mean slope of the hillside is  $-\bar{U}$  and the stagnant zones, with constant  $\bar{U}y - \bar{\psi}$ , are the flat terraces carved into the hillside. The existence of these stagnant pools is explained by the closed-streamline theorem of appendix B. The stagnant pools are separated by boundary layers and the strongest of these is main channel which appears as the large cliff located roughly at  $y/L = \pi/2$  in figure 4(b). The main channel is determined by a narrow band of geostrophic contours that are opened by the small  $\beta$ -effect: this provides an open path for flow through the disordered topography.

### 3.3. An example with open geostrophic contours: $\beta\ell_\eta/\eta_{\text{rms}} = 1.38$

Figures 5 and 6 show a solution for a case with  $\beta\ell_\eta/\eta_{\text{rms}} = 1.38$ ,  $F/(\mu\eta_{\text{rms}}\ell_\eta) = 26.09$  and  $\mu/\eta_{\text{rms}} = 0.01$ ; the geostrophic contours are open throughout the domain. The most striking difference when compared to the previous case in section 3.2 is that there are no stagnant zones; the flow is more evenly spread throughout the domain: compare figure 6 with figure 4. The time mean streamfunction in figure 6(b) is not ‘‘terraced’’. Instead  $\bar{\psi} - \bar{U}y$  in figure 6(b) is better characterized as a bumpy hillside.

In this example the large-scale flow is  $\bar{U} = 6.46 \text{ cm s}^{-1}$ , which is again very much smaller than the flow that would exist in the absence of topography:  $\bar{U}$  is only 0.7% of  $F/\mu$ . The eddy energy  $E_\psi$  is roughly 120 times larger than the large-scale flow energy  $E_U$ . Moreover, in this case, the energy of the transient eddies, shown in figure 5(b), is much larger than that of the standing eddies. This is also apparent by comparing the instantaneous and time-mean relative vorticity fields in figures 5(c) and (d). In anticipation of the discussion in section 8 we remark that these strong transient eddies act as PV diffusion on the time-mean QGPV (Rhines & Young 1982).

Again we find that the relative vorticity is anti-correlated with the topographic PV,

$$\langle \bar{\zeta}\eta \rangle / \sqrt{\langle \bar{\zeta}^2 \rangle \langle \eta^2 \rangle} = -0.25, \quad (3.8)$$

but, in contrast to the previous example in section 3.2, the negative  $\bar{\zeta}-\eta$  correlation is not apparent by visual inspection of figures 5(c) and (d). The correlation of the standing streamfunction with the topographic PV gradient is larger for this case:

$$\langle \bar{\psi}\eta_x \rangle / \sqrt{\langle \bar{\psi}^2 \rangle \langle \eta_x^2 \rangle} = 0.32.$$

Again it is remarkable that this rather weak correlation is sufficient to produce a form stress balancing 99.3% of the wind stress.

### 3.4. Relation between QGPV and total streamfunction

Figure 7 shows scatter plots of the time-mean QGPV,  $\bar{q} + \beta y$ , versus the time-mean streamfunction  $\bar{\psi} - \bar{U}y$ , for the two examples of sections 3.2 and 3.3. In the case with closed geostrophic contours the terraces in figure 4(b), or equivalently the stagnant zones in figure 4(a), can be identified by the series of near vertical lines in figure 7(a). On the other hand, in the case with open geostrophic contours figure 7(b) shows a series of nearly horizontal cusps indicating a tendency towards homogenization of QGPV. Homogenization is discussed further in section 8.

Earlier theoretical arguments by Salmon *et al.* (1976) and Bretherton & Haidvogel (1976) based on equilibrium statistical mechanics or unforced initial value problems have indicated that there might be a tight functional relationship between the QGPV and streamfunction: this is not a good characterization of the multi-branched relations that characterize the forced-dissipative solutions discussed here.

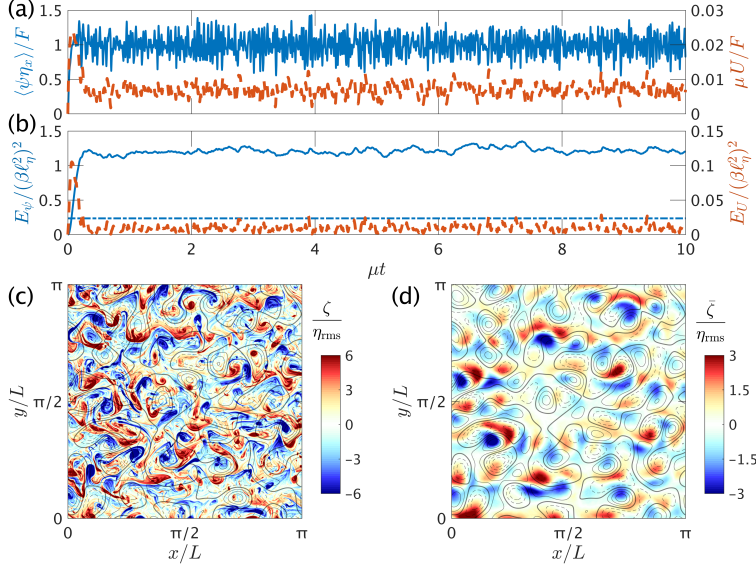


Figure 5: A solution with  $\beta\ell_\eta/\eta_{rms} = 1.38$  and  $F/(\mu\eta_{rms}\ell_\eta) = 26.09$ . Panels as in figure 3. Note that the color scale is different between panels (c) and (d). A movie showing the evolution of  $\zeta$  and  $\psi$  from rest can be found in **Supplementary Materials**.

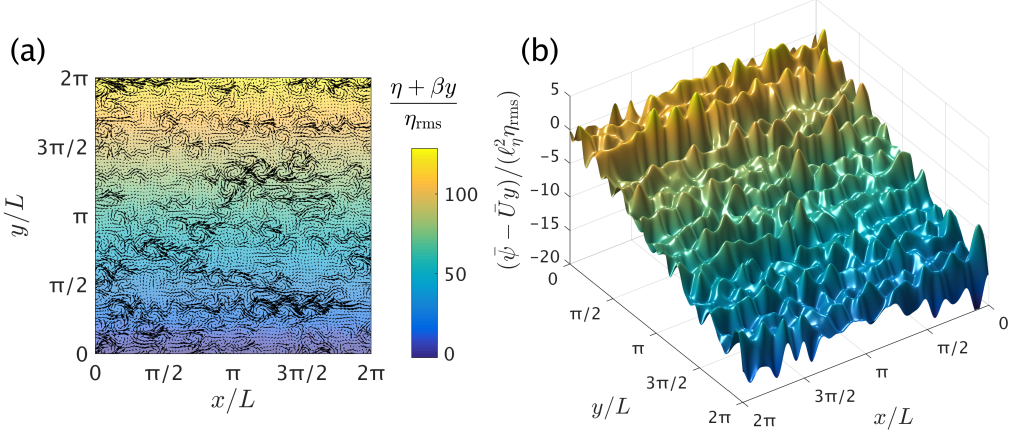


Figure 6: A solution with  $\beta\ell_\eta/\eta_{rms} = 1.38$  and  $F/(\mu\eta_{rms}\ell_\eta) = 26.09$ . (a) The environmental PV,  $\eta + \beta y$ , (shaded) and the time-mean velocity field,  $\bar{U}$ , as arrows. (b) Surface plot of the total time-mean streamfunction,  $\bar{\psi} - \bar{U}y$ .

#### 4. Flow regimes and a parameter survey

In this section we present a comprehensive suite of numerical simulations of (2.4) and (2.6) using the topography of figure 1(a). A complete survey of the parameter space is complicated by the existence of at least four control parameters. There are four time scales in the problem: the topographic PV  $\eta_{rms}^{-1}$ , the dissipation  $\mu^{-1}$ , the period of topographically excited Rossby waves  $(\beta\ell_\eta)^{-1}$ , and the advective time-scale associated with the forcing  $\ell_\eta\mu/F$ . From these four time scales we construct the three main control

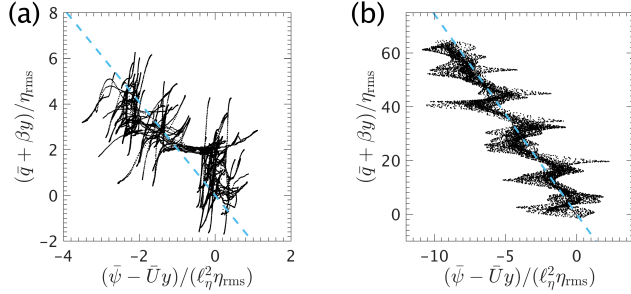


Figure 7: Scatter plots of the time-mean QGPV,  $\bar{q} + \beta y$ , versus the time-mean total streamfunction,  $\bar{\psi} - \bar{U}y$  for the solutions shown in figures 4 and 6. The dashed lines mark the slope  $-\beta/\bar{U}$ . (a)  $\beta\ell_\eta/\eta_{rms} = 0.1$ ; (b)  $\beta\ell_\eta/\eta_{rms} = 1.38$ .

parameters:

$$\frac{\mu}{\eta_{rms}}, \quad \frac{\beta\ell_\eta}{\eta_{rms}} \quad \text{and} \quad \frac{F}{\mu\eta_{rms}\ell_\eta}. \quad (4.1)$$

There is a fourth parameter  $L/\ell_\eta$  that measures the scale separation between the domain and the topography. We assume that as  $L/\ell_\eta \rightarrow \infty$  there is a regime of statistically homogeneous two-dimensional turbulence. In other words, as  $L/\ell_\eta \rightarrow \infty$ , the flow becomes asymptotically independent of  $L/\ell_\eta$  so that the large-scale flow  $\bar{U}$  and other statistics, such as  $E_{\bar{\psi}}$ , are independent of the domain size  $L$ .

In addition to the four parameters above, additional parameters are required to characterize the topography. For example, in the case of a multi-scale topography the ratio  $L_\eta/\ell_\eta$  characterizes the spectral width of the power-law range. A main simplification of the monoscale case used throughout this paper is that we do not have to contend with these additional topographic parameters.

In the following survey we use

$$\mu/\eta_{rms} = 10^{-2}, \quad (4.2)$$

and vary the strength of the large-scale wind forcing  $F$  and the planetary vorticity gradient  $\beta$ . Most of these solutions use  $512^2$  grid points; additionally, a few  $1024^2$  solutions were obtained to test sensitivity to resolution (we found none). Unless stated otherwise, numerical simulations are initiated from rest and time-averaged quantities are calculated by averaging the fields over the interval  $10 \leq \mu t \leq 30$ .

#### 4.1. Flow regimes: the lower branch, the upper branch, eddy saturation and the drag crisis

Keeping  $\beta$  fixed and increasing the wind forcing,  $F$ , from very small values we find that the statistically equilibrated solutions show either one of the two characteristic behaviors depicted in figure 8.

For  $\beta = 0$ , or for values of  $\beta\ell_\eta/\eta_{rms}$  much less than one, we find that the equilibrated time-mean large-scale flow,  $\bar{U}$  scales linearly with  $F$  when  $F$  is very small. On this “lower branch” the large-scale velocity is

$$\bar{U} \approx F/\mu_{\text{eff}}, \quad \text{with} \quad \mu_{\text{eff}} \gg \mu. \quad (4.3)$$

In section 6 we provide an analytic expression for the effective drag  $\mu_{\text{eff}}$  in (4.3); this analytic expression is shown by the dashed lines in figure 8. As  $F$  increases,  $\bar{U}$  transitions

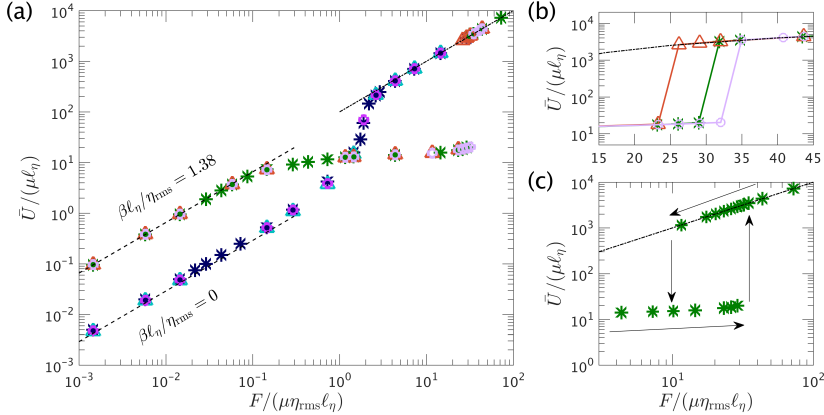


Figure 8: (a) The equilibrated large-scale mean flow  $\bar{U}$  scaled with  $\mu\ell_\eta$  as a function of the non-dimensional forcing  $F/(\mu\eta_{\text{rms}}\ell_\eta)$  with  $\beta\ell_\eta/\eta_{\text{rms}} = 0$  and  $\beta\ell_\eta/\eta_{\text{rms}} = 1.38$ . Shown are results for three different monoscale topography realizations (each denoted with a different marker symbol: \*,  $\Delta$ ,  $\circ$ ) all with the spectrum shown in figure 1(c). Other parameters are in Table 2 e.g.,  $\mu/\eta_{\text{rms}} = 10^{-2}$ . Dashed lines in panel (a) correspond to asymptotic expressions derived in section 6 and dash-dotted lines in all panels mark the solution:  $U = F/\mu$ . Panel (b) shows a detailed view of the transition from the lower to the upper branch solution for the case with  $\beta\ell_\eta/\eta_{\text{rms}} = 1.38$  and panel (c) shows the hysteretic solutions for one of the topography realizations with  $\beta\ell_\eta/\eta_{\text{rms}} = 1.38$ .

to a different linear relation with

$$\bar{U} \approx F/\mu. \quad (4.4)$$

On this ‘‘upper branch’’ the form stress is essentially zero and  $F$  is balanced only by bare drag  $\mu$ . For the  $\beta = 0$  case shown in figure 8 the transition between the lower and upper branch occurs in the range  $0.6 < F/(\mu\eta_{\text{rms}}\ell_\eta) < 3$ ; the equilibrated  $\bar{U}$  increases by a factor of more than 200 within this interval.

On the other hand, for  $\beta\ell_\eta/\eta_{\text{rms}}$  larger than 0.05, we find a quite different behavior, illustrated in figure 8 by the runs with  $\beta\ell_\eta/\eta_{\text{rms}} = 1.38$ . On the lower branch  $\bar{U}$  grows linearly with  $F$  with a constant  $\mu_{\text{eff}}$  as in (4.3). But the linear increase in  $\bar{U}$  eventually ceases and instead  $\bar{U}$  then grows at a much more slower rate as  $F$  increases. For the case  $\beta\ell_\eta/\eta_{\text{rms}} = 1.38$  shown in figure 8,  $\bar{U}$  only doubles as  $F$  is increased over 100-fold from  $F/(\mu\eta_{\text{rms}}\ell_\eta) = 0.2$  to 30. We identify this regime, in which  $\bar{U}$  is insensitive to changes in  $F$ , with the ‘‘eddy saturation’’ regime of Straub (1993). As  $F$  increases further the flow exits the eddy saturation regime via a ‘‘drag crisis’’ in which the form stress abruptly vanishes and  $\bar{U}$  increases by a factor of over 200 as the solution jumps to the upper branch (4.4). In figure 8 this drag crisis is a discontinuous transition from the eddy saturated regime to the upper branch. The drag crisis, which requires non-zero  $\beta$ , is qualitatively different from the continuous transition between the upper and lower branches which is characteristic of flows with small (or zero)  $\beta\ell_\eta/\eta_{\text{rms}}$ .

Figure 8 shows results obtained with three different realizations of monoscale topography viz., the topography illustrated in figure 1(a) and two other realizations with the monoscale spectrum of figure 1(b). The large-scale flow  $\bar{U}$  is insensitive to these changes in topographic detail; in this sense the large-scale flow is ‘‘self-averaging’’. However the precise location of the drag crisis depends slightly on differences between the three realizations: panel (b) of figure 8 shows that the location of the jump from lower to upper branch is realization

dependent: the three different realizations of the topography jump to the upper branch at rather different values of  $F/(\mu\eta_{\text{rms}}\ell_\eta)$ .

The case with  $\beta\ell_\eta/\eta_{\text{rms}} = 0.1$ , which corresponds a value close to realistic (cf. Table 2), does show a drag crisis, i.e., a discontinuous jump from the lower to the upper branch at  $F/(\mu\eta_{\text{rms}}\ell_\eta) \approx 3.9$ . However, the eddy saturation regime, i.e., the regime in which  $\bar{U}$  is insensitive to changes in wind stress, is not nearly as pronounced as in the case with  $\beta\ell_\eta/\eta_{\text{rms}} = 1.38$  shown in figure 8(a).

#### 4.2. Hysteresis and multiple flow patterns

Starting with a severely truncated spectral model of the atmosphere introduced by Charney & DeVore (1979), there has been considerable interest in the possibility that topographic form stress might result in multiple stable large-scale flow patterns and that this might explain blocked and unblocked states of atmospheric circulation. Focussing on atmospheric conditions, Tung & Rosenthal (1985) concluded that the results of low-order truncated models are not a reliable guide to the full nonlinear problem: although multiple stable states still exist in the full problem, these occur only in a restricted parameter range that is not characteristic of Earth's atmosphere.

With this meteorological background in mind, it is interesting that in the oceanographic parameter regime emphasized here, we easily found multiple equilibrium solutions on either side of the drag crisis. After increasing  $F$  beyond crisis point, and jumping to the upper branch, we performed additional numerical simulations by decreasing  $F$  and using initial conditions obtained from the upper-branch solutions at larger values of  $F$ . Thus we moved down the upper branch, past the crisis, and determined a range of  $F$ 's with multiple flow patterns. Panel (c) of figure 8, with  $\beta\ell_\eta/\eta_{\text{rms}} = 1.38$ , shows that multiple states co-exist in the range  $11 \leq F/(\mu\eta_{\text{rms}}\ell_\eta) \leq 29$ . Note that for quasi-realistic case with  $\beta\ell_\eta/\eta_{\text{rms}} = 0.1$  multiple solutions exist only in the limited parameter range  $2.9 \leq F/(\mu\eta_{\text{rms}}\ell_\eta) \leq 3.9$  (i.e., for wind stress values between  $0.26 \text{ N m}^{-2}$  and  $0.35 \text{ N m}^{-2}$ ). These co-existing flows differ qualitatively: the lower-branch flows, being near the drag crisis, have an important transient eddy component and almost all of  $F$  is balanced by form stress: the example discussed in connection with figures 3 and 4 is typical. On the other hand, the co-existing upper-branch solutions are steady (that is  $\psi' = U' = 0$ ) and nearly all of the wind stress is balanced by bottom drag so that  $\mu U/F \approx 1$ .

#### 4.3. A survey

In this section we present a suite of solutions, all with  $\mu/\eta_{\text{rms}} = 10^{-2}$ . The main conclusion from these extensive calculations is that the behavior illustrated in figure 8 is representative of a broad region of parameter space. Figure 9(a) shows the ratio  $\mu\bar{U}/F$  as a function of  $F/(\mu\eta_{\text{rms}}\ell_\eta)$  for seven different values of  $\beta$ . The three series with  $\beta\ell_\eta/\eta_{\text{rms}} \leq 0.10$  are “small- $\beta$ ” cases in which closed geostrophic contours fill most of the domain; the other four series, with  $\beta\ell_\eta/\eta_{\text{rms}} \geq 0.35$ , are “large- $\beta$ ” cases in which open geostrophic contours fill most of the domain. For small values of  $F/(\mu\eta_{\text{rms}}\ell_\eta)$  in figure 9(a) the flow is steady ( $\psi' = U' = 0$ ) and  $\mu\bar{U}/F$  does not change with  $F$ : this is the lower-branch relation (4.3) in which  $\bar{U}$  varies linearly with  $F$  with an effective drag coefficient  $\mu_{\text{eff}}$ . As  $F/(\mu\eta_{\text{rms}}\ell_\eta)$  is increased, this steady flow becomes unstable and the strength of the transient eddy field increases with  $F$ .

Figure 9(b) shows a detailed view of the eddy saturation regime and the drag crisis. The dashed lines in the left of figure 9(a) show the analytic results of (6.4) for  $\beta\ell_\eta/\eta_{\text{rms}} \geq 0.35$  while the dashed line in figure 9(b) shows result (6.11). Figure 9(b) shows a detailed view of the eddy saturation regime and the drag-crisi. For the large- $\beta$  cases the form stress

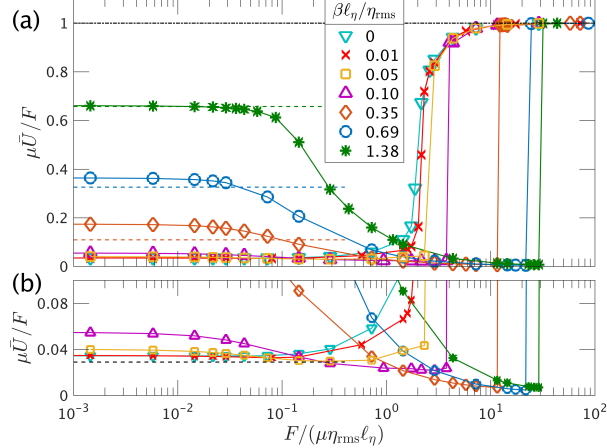


Figure 9: Panel (a) shows the ratio  $\mu\bar{U}/F$  as a function of the non-dimensional forcing,  $F/(\mu\eta_{\text{rms}}\ell_\eta)$ , for seven values of  $\beta\ell_\eta/\eta_{\text{rms}}$ . Panel (b) shows a detailed view of the eddy saturation regime and the drag crisis.

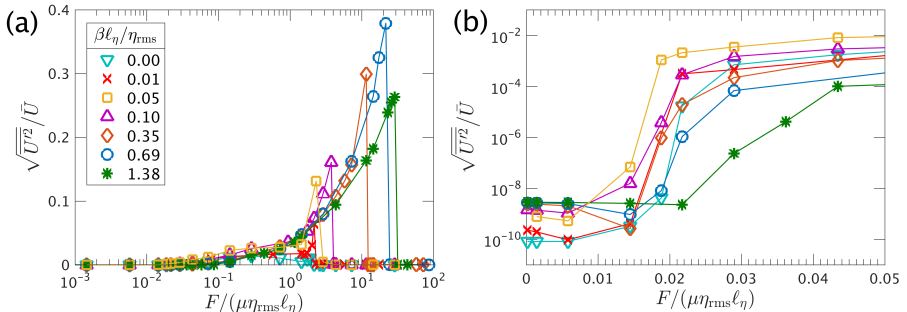


Figure 10: (a) The index in (4.5) measures the strength of the transient eddies as a function of the non-dimensional  $F$ . Panel (b) shows a detailed view of the onset of transient eddies.

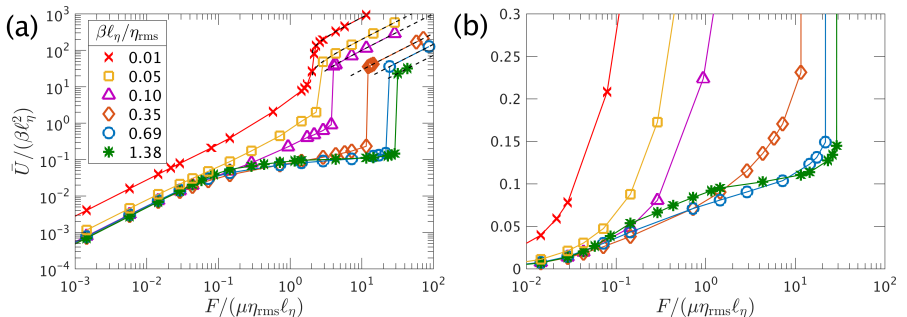


Figure 11: (a) The equilibrated large-scale flow,  $\bar{U}$ , scaled with  $\beta\ell_\eta^2$  as a function of the non-dimensional forcing for various values of  $\beta\ell_\eta/\eta_{\text{rms}}$ . Dashed curves indicate upper branch analytic result from section 7 (also scaled with  $\beta\ell_\eta^2$ ). (b) An expanded view showing the eddy saturation regime.

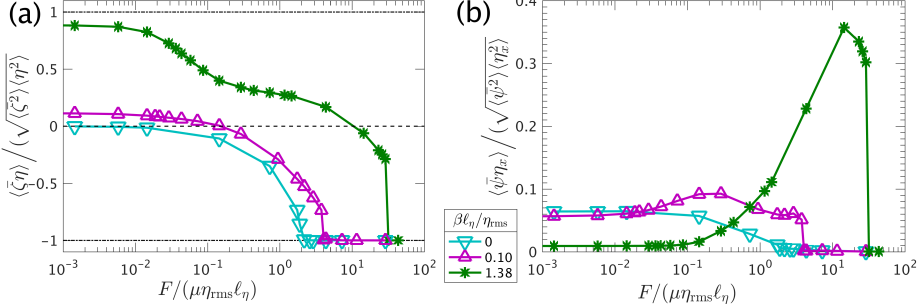


Figure 12: (a) Correlation of the standing eddy vorticity  $\bar{\zeta}$  with the topographic PV  $\eta$  for  $\beta\ell_\eta/\eta_{\text{rms}} = 0, 0.10$  and  $1.38$ . For  $\beta\ell_\eta/\eta_{\text{rms}} = 0$  the correlations between  $\bar{\zeta}$  and  $\eta$  is always negative: for  $F/(\mu\eta_{\text{rms}}\ell_\eta) = 10^{-3}$ ,  $\langle \bar{\zeta}\eta \rangle / \sqrt{\langle \bar{\zeta}^2 \rangle} \sqrt{\langle \eta^2 \rangle} = -1.35 \times 10^{-3}$ . (b) Correlation of  $\bar{\psi}$  with  $\eta_x$ .

makes a very large contribution to the large-scale momentum balance prior the drag crisis. For the runs with  $\beta\ell_\eta/\eta_{\text{rms}} \geq 0.35$ , as much as 99.5% of  $F$  is balanced by  $\langle \bar{\psi}\eta_x \rangle$ ; in the case with  $\beta\ell_\eta/\eta_{\text{rms}} = 0.1$  over 95% of  $F$  is balanced by  $\langle \bar{\psi}\eta_x \rangle$ . We emphasize that although drag  $\mu$  does not directly balance  $F$  in this regime, it does play a crucial role in producing non-zero form stress  $\langle \bar{\psi}\eta_x \rangle$ . In all of the solutions summarized in figure 9, non-zero  $\mu$  is required so that the flow is asymmetric upstream and downstream of topographic features; this asymmetry induces non-zero  $\langle \bar{\psi}\eta_x \rangle$ .

In figure 10 we use

$$\sqrt{\bar{U}^2} / \bar{U} \quad (4.5)$$

as an indication of the onset of the transient-eddy instability and as an index of the strength of the transient eddies. Remarkably, the onset of the instability is roughly at  $F/(\mu\eta_{\text{rms}}\ell_\eta) = 1.5 \times 10^{-2}$  for all values of  $\beta\ell_\eta/\eta_{\text{rms}}$ : the onset of transient eddies is the sudden increase in (4.5) by a factor of about  $10^4$  or  $10^5$  in figure 10(b). The transient eddies result in reduction of  $\mu\bar{U}/F$ ; for the large- $\beta$  runs, this is the eddy saturation regime. In the presentation in figure 9(a) the eddy saturation regime is the decease in  $\mu\bar{U}/F$  that occurs once  $0.03 < F/(\mu\eta_{\text{rms}}\ell_\eta) < 0.3$  (depending on  $\beta\ell_\eta/\eta_{\text{rms}}$ ). The eddy saturation regime is terminated by the drag-crisis jump to the upper branch where  $\mu\bar{U}/F \approx 1$ . This coincides with vanishing of the transients: on the upper branch the flow becomes steady:  $\psi' = U' = 0$ : see figure 10(a).

Figure 11 shows the eddy saturation regime that is characteristic of the three series with  $\beta\ell_\eta/\eta_{\text{rms}} \geq 0.35$ . Eddy saturation occurs for forcing in the range

$$0.1 \lesssim F/(\mu\eta_{\text{rms}}\ell_\eta) \lesssim 30;$$

in this regime the large-scale flow is limited to the relatively small range

$$0.06 \beta\ell_\eta^2 \lesssim \bar{U} \lesssim 0.25 \beta\ell_\eta^2.$$

In anticipation of analytic results from the next section we note that in the relation above,  $\beta\ell_\eta^2$  is the speed of Rossby waves excited by this topography with typical length scale  $\ell_\eta$ .

Figure 12 shows the correlations  $\langle \bar{\zeta}\eta \rangle$  and  $\langle \bar{\psi}\eta_x \rangle$  as a function of the forcing  $F/(\mu\eta_{\text{rms}}\ell_\eta)$  for three values of  $\beta\ell_\eta/\eta_{\text{rms}}$ :  $\beta\ell_\eta/\eta_{\text{rms}} = 0$  and  $\beta\ell_\eta/\eta_{\text{rms}} = 0.10$  which correspond to closed geostrophic contours and  $\beta\ell_\eta/\eta_{\text{rms}} = 1.38$  which corresponds to open geostrophic contours. In most weakly forced cases  $\bar{\zeta}$  is positively correlated with the topographic PV  $\eta$ ;

as the forcing  $F$  increases,  $\bar{\zeta}$  and  $\eta$  become anti-correlated. However, for  $\beta\ell_\eta/\eta_{\text{rms}} = 0$  then  $\langle\bar{\zeta}\eta\rangle$  is negative for all values of  $F$ : for  $\beta\ell_\eta/\eta_{\text{rms}} = 0$  the term  $\langle\eta D\bar{\zeta}\rangle$  in the time-average of (2.10b) is the only source of enstrophy and therefore  $\langle\bar{\zeta}\eta\rangle$  must be negative.

## 5. A quasilinear (QL) theory

A prediction of the statistical steady state of (2.4) and (2.6) was first made by [Davey \(1980\)](#). In this section we present Davey's quasilinear (QL) theory and in subsequent sections explore its validity in various regimes documented in section 4. This QL theory, although it refers to steady solutions, neglecting transient components, still captures the effect of the topographic wave drag due to stationary Rossby waves.

Assume that the QGPV equation (2.4) has a steady solution and also neglect the term  $J(\psi, q) = J(\psi, \eta) + J(\psi, \zeta)$ . These approximations result in the QL QGPV equation

$$U\zeta_x + \beta\psi_x + \mu\zeta = -U\eta_x, \quad (5.1)$$

in which  $U$  is determined by the steady mean flow equation

$$F - \mu U - \langle\psi\eta_x\rangle = 0. \quad (5.2)$$

In (5.1) we have neglected lateral dissipation so that the dissipation is  $D = \mu$ . Notice that the only nonlinear term in (5.1) is  $U\zeta_x$ . Regarding  $U$  as an unknown parameter, the solution of (5.1) is:

$$\psi = U \sum_{\mathbf{k}} \frac{ik_x \eta_{\mathbf{k}} e^{i\mathbf{k}\cdot\mathbf{x}}}{\mu|\mathbf{k}|^2 - ik_x(\beta - |\mathbf{k}|^2 U)}. \quad (5.3)$$

Thus the QL approximation to the form stress in (5.2) is

$$\langle\psi\eta_x\rangle = U \sum_{\mathbf{k}} \frac{\mu k_x^2 |\mathbf{k}|^2 |\eta_{\mathbf{k}}|^2}{\mu^2 |\mathbf{k}|^4 + k_x^2 (\beta - |\mathbf{k}|^2 U)^2}. \quad (5.4)$$

Inserting (5.4) into the large-scale momentum equation (5.2) one obtains an equation for  $U$ . This equation is a polynomial of order  $2N + 1$ , where  $N \gg 1$  is the number of non-zero terms in the sum in (5.4). This implies, at least in principle, that there might be many real solutions for  $U$ . However, for the monoscale topography of figure 1, we usually find either one real solution or three as  $F$  is varied: see figure 13(a). In a very limited parameter region we find a multitude of additional real solutions: see figure 13(b). The fine-scale features evident in figure 13(b) vary greatly between different realizations of the topography and are irrelevant for the full nonlinear system.

For the special case of isotropic monoscale topography we simplify (5.4) by converting the sum over  $\mathbf{k}$  into an integral that can be evaluated analytically (see appendix C). The result is

$$\langle\psi\eta_x\rangle = \frac{\mu\eta_{\text{rms}}^2 \ell_\eta^2 U}{\mu^2 \ell_\eta^2 + (\beta\ell_\eta^2 - U)^2 + \mu\ell_\eta \sqrt{\mu^2 \ell_\eta^2 + (\beta\ell_\eta^2 - U)^2}}. \quad (5.5)$$

Expression (5.5) is a good approximation to the sum (5.4) for the monoscale topography of figure 1(a), which has power over an annular region in wavenumber space with width  $\Delta k L \approx 8$ . The dashed curves in figure 13 are obtained by solving the mean-flow equation (5.2) with form stress given by the analytic expression in (5.5); there is good agreement with the sum (5.4) except in the small regions shown in panels (b) and (c) where the resonances of the denominator come into play. This comparison shows that the form stress produced in a single realization of random topography is self-averaging

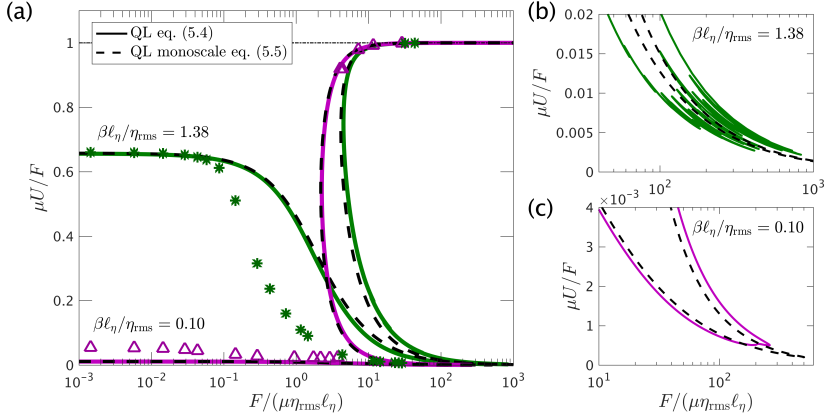


Figure 13: (a) The large-scale flow,  $\mu \bar{U}/F$ , as a function of forcing the  $F/(\mu \eta_{\text{rms}} \ell_\eta)$  for the cases with  $\beta \ell_\eta / \eta_{\text{rms}} = 0.10$  and  $1.38$ . The solid curves are the QL predictions using a single realization to evaluate the sum in (5.4) and the dashed curves are the ensemble-average predictions from (5.5); the markers indicate the numerical solution of the full nonlinear system (2.4) and (2.6). Panels (b) and (c) show a detailed view on the bottom right corner of panel (a), where the resonances in the denominator of (5.4) come into play.

i.e., the ensemble average in (5.5) is close to the result obtained by evaluating the sum in (5.4) using a single realization of the  $\eta_k$ 's.

Figure 13 also compares the QL prediction in (5.4) and (5.5) to solutions of the full system. Regarding weak forcing,  $F/(\mu \eta_{\text{rms}} \ell_\eta) \ll 1$ , the QL approximation seriously underestimates  $\mu U/F$  for the case with  $\beta \ell_\eta / \eta_{\text{rms}} = 0.1$  in figure 13. The failure of the QL approximation in this case with dominantly closed geostrophic contours is expected because the important term  $J(\psi, \eta)$  is discarded in (5.1). On the other hand, the QL approximation has some success for the case with  $\beta \ell_\eta / \eta_{\text{rms}} = 1.38$ : proceeding in figure 13 from very small  $F/(\mu \eta_{\text{rms}} \ell_\eta)$ , we find close agreement till about  $F/(\mu \eta_{\text{rms}} \ell_\eta) \approx 0.1$ . At that point the QL approximation departs from the full solution: the velocity  $U$  predicted by the QL approximation is greater than the actual velocity, meaning that the QL form stress  $\langle \bar{\psi} \eta_x \rangle$  is too small. This failure of the QL approximation is clearly associated with the linear instability of the steady solution and the development of transient eddies: the nonlinear results for the  $\beta \ell_\eta / \eta_{\text{rms}} = 1.38$  case in figure 13(a) first depart from the QL approximation when the index (4.5) signals the onset of unsteady flow. This failure of the QL theory due to transient eddies will be further discussed in section 8. For strong forcing ( $F/(\mu \eta_{\text{rms}} \ell_\eta) \gg 1$ ), the QL approximation predicts very well the upper branch solution.

While the assumptions leading to the QL estimate (5.4) are drastic, as we will see in sections 6 and 7, the QL approximation captures the qualitative behavior of the full numerical solution and, in some parameter regimes such as  $\beta \ell_\eta / \eta_{\text{rms}} \gtrsim 1$ , even provides a good quantitative prediction of  $\bar{U}$ .

## 6. The weakly forced regime, $F/(\mu \eta_{\text{rms}} \ell_\eta) \ll 1$

In this section we consider the weakly forced case. In figures 8 and 9 this regime is characterized by the “effective drag”  $\mu_{\text{eff}}$  in (4.3). Our main goal here is to determine  $\mu_{\text{eff}}$  in the weakly forced regime.

In the linear limit  $F \rightarrow 0$  the nonlinear terms are negligible and the eddy field satisfies

the simplified equation:

$$J(\psi, \eta) + \beta\psi_x + \mu\zeta = -U\eta_x. \quad (6.1)$$

Comparing (6.1) with the QL approximation in (5.1) we see that (6.1) contains the additional linear term  $J(\psi, \eta)$  and does not contain the term  $U\zeta_x$ , which is quadratic in flow fields. We regard the right hand side of the linear equation (6.1) as a forcing term that generates the streamfunction  $\psi$ .

### 6.1. The case with either $\mu/\eta_{\text{rms}} \gg 1$ or $\beta\ell_\eta/\eta_{\text{rms}} \gg 1$

Assuming that lengths scale with  $\ell_\eta$ , the ratio of the terms on the left of (6.1) is:

$$\frac{\beta\psi_x}{J(\psi, \eta)} = O\left(\frac{\beta\ell_\eta}{\eta_{\text{rms}}}\right) \quad \text{and} \quad \frac{\mu\zeta}{J(\psi, \eta)} = O\left(\frac{\mu}{\eta_{\text{rms}}}\right). \quad (6.2)$$

If

$$\mu/\eta_{\text{rms}} \gg 1, \quad \text{or if} \quad \beta\ell_\eta/\eta_{\text{rms}} \gg 1, \quad (6.3)$$

then  $J(\psi, \eta)$  is negligible relative to one, or both, of the other two terms on the left hand side of (6.1). If the first inequality is satisfied then the solution of (6.1) is determined by a two-term balance between the drag term and the forcing on the right. If the second inequality in (6.3) is satisfied then the topographic PV gradient is much less than  $\beta$  and the two-term balance is between  $\beta\psi_x$  and forcing on the right of (6.1).

Thus, provided that (6.3) applies, one can neglect the Jacobian in (6.1) and adapt the QL expression (5.5) to determine the effective drag of monoscale topography as

$$\mu_{\text{eff}} = \mu + \frac{\mu\eta_{\text{rms}}^2\ell_\eta^2}{\mu^2\ell_\eta^2 + \beta^2\ell_\eta^4 + \mu\ell_\eta\sqrt{\mu^2\ell_\eta^2 + \beta^2\ell_\eta^4}}. \quad (6.4)$$

In simplifying the QL expression (5.5) to the linear result (6.4) we have neglected  $U$  relative to either  $\beta\ell_\eta^2$  or  $\mu\ell_\eta$ : this simplification is appropriate in the limit  $F \rightarrow 0$ . The expression in (6.4) is accurate within the shaded region in figure 14. The dashed lines in figures 8 and 9 that correspond to the series with  $\beta\ell_\eta/\eta_{\text{rms}} \geq 0.35$  indicate the approximation  $\bar{U} \approx F/\mu_{\text{eff}}$  with  $\mu_{\text{eff}}$  in (6.4).

### 6.2. The thermal analogy — the case with $\mu/\eta_{\text{rms}} \lesssim 1$ and $\beta\ell_\eta/\eta_{\text{rms}} \lesssim 1$

When both  $\mu/\eta_{\text{rms}}$  and  $\beta\ell_\eta/\eta_{\text{rms}}$  are order one or less, the term  $J(\psi, \eta)$  in (6.1) cannot be neglected. As a result of this Jacobian, the weakly forced regime cannot be recovered as a special case of the QL approximation. In this interesting case we rewrite (6.1) as

$$J(\eta + \beta y, \psi - Uy) = \mu\nabla^2\psi, \quad (6.5)$$

and rely on intuition based on the “thermal analogy” of Welander (1968). To apply the analogy we regard  $\eta + \beta y$  as an effective steady streamfunction advecting a passive scalar  $\psi - Uy$ . The planetary vorticity gradient  $\beta$  is analogous to a large-scale zonal flow  $-\beta$  and the large-scale flow  $U$  is analogous to a large-scale tracer gradient; the drag  $\mu$  is equivalent to the diffusivity of the scalar. The form stress  $\langle\psi\eta_x\rangle$  is analogous to the meridional flux of tracer  $\psi$  by the meridional velocity  $\eta_x$ . To make the dimensions consistent with the conventional passive-scalar problem one might multiply (6.5) by  $(\mu/\beta)^2$ . Then, for instance, the diffusivity is  $\mu^3/\beta^2$  with dimensions  $(\text{length})^2(\text{time})^{-1}$ . We prefer to use (6.5) and tolerate the unconventional units. Usually in the passive-scalar problem the large-scale tracer gradient  $U$  is imposed and the main goal is to determine the flux  $\langle\psi\eta_x\rangle$  (equivalently the Nusselt number). But here,  $U$  is unknown and must be

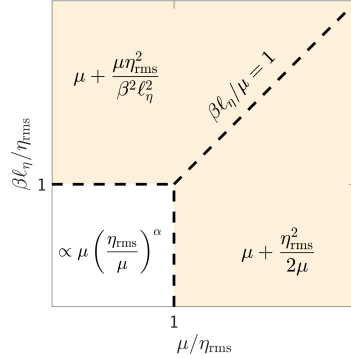


Figure 14: Schematic for the three different parameter regions in the weakly forced regime. Shaded region depicts the parameter range for which the QL theory gives good predictions. For  $\beta\ell_\eta/\eta_{rms} < 1$  and  $\mu/\eta_{rms} < 1$  the form stress and the large-scale flow largely depend on the actual geometry of the topography and insight can be obtained from percolation theory. The expressions depict the behavior of  $\mu_{\text{eff}}$  in each parameter region.

determined by satisfying the steady version of the large-scale momentum equation (5.2). Geostrophic contours are equivalent to streamlines in the thermal analogy.

We now show that in the limit  $\mu/\eta_{rms} \rightarrow 0$  the total streamfunction,  $\psi - Uy$  is constant within any closed geostrophic contours i.e., all parts of the domain contained within closed geostrophic contours are stagnant. We assume a regular perturbation series expansion for  $\psi$  in powers of  $\epsilon = \mu/\eta_{rms}$ :  $\psi = \psi_0 + \epsilon^1\psi_1 + \epsilon^2\psi_2 + \dots$ . The zeroth order of (6.5) is then:

$$J(\eta + \beta y, \psi_0 - Uy) = 0. \quad (6.6)$$

The general solution of (6.6) is

$$\psi_0 - Uy = \mathcal{F}(\eta + \beta y), \quad (6.7)$$

where  $\mathcal{F}$  is an undetermined function. At next order,  $\epsilon^1$ , one has:

$$J(\eta + \beta y, \psi_1) = \mu \nabla^2 (\psi_0 - Uy). \quad (6.8)$$

Using the argument from appendix B, the integral of  $J(\eta + \beta y, \psi_1)$  over the area enclosed by a geostrophic contour identically vanishes, and

$$\nabla(\psi_0 - Uy) = \mathcal{F}' \nabla(\eta + \beta y) = \mathcal{F}' |\nabla(\eta + \beta y)| \hat{n}, \quad (6.9)$$

where  $\mathcal{F}'$  is the derivative of  $\mathcal{F}$  and  $\hat{n}$  is the unit normal to the geostrophic contour. Thus integrating (6.8) over the area contained within any closed geostrophic contour we obtain:

$$\mu \oint |\nabla(\eta + \beta y)| d\ell \mathcal{F}' = 0. \quad (6.10)$$

This implies that  $\mathcal{F}' = 0$  or equivalently that  $\mathcal{F}$  is constant within any closed geostrophic contour i.e., the region within closed geostrophic contours is stagnant.

This conclusion is illustrated in figures 15 which shows a weakly forced, small-drag solution with  $\beta\ell_\eta/\eta_{rms} = 0$ . The characteristic “terraced hillside” in figure 15(c) is even more striking than in figure 4: the solution in figure 4 has transient eddies resulting in a blurring of the terraced structure. The weakly-forced solution in figure 15 is steady and the thickness of the steps between the terraces is limited only by the small drag,  $\mu/\eta_{rms} = 1/200$ .

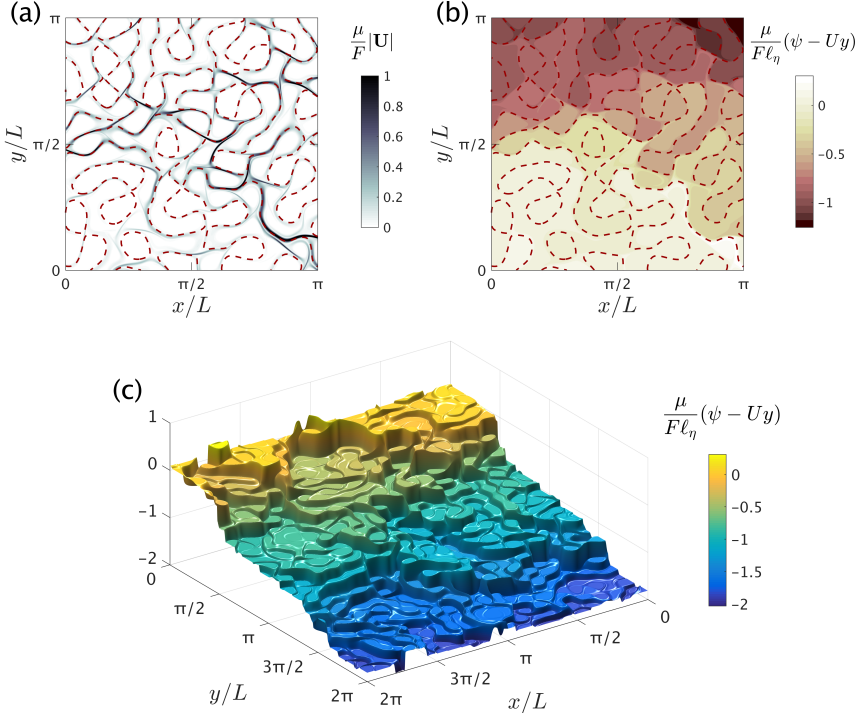


Figure 15: Snapshots of flow fields for weakly forced simulations at  $F/(\mu \eta_{\text{rms}} \ell_\eta) = 10^{-3}$  with dissipation  $\mu/\eta_{\text{rms}} = 5 \times 10^{-3}$  and planetary vorticity gradient  $\beta \ell_\eta/\eta_{\text{rms}} = 0$ . (a) The total velocity magnitude  $|\mathbf{U}|$ . The flow is restricted to a boundary layer around the dashed  $\eta = 0$  contour. (b) The total streamfunction  $\psi - Uy$  for the solution in panel (a). (c) Surface plot of the total streamfunction,  $\psi - Uy$ . The terraced hillside structure is apparent. (In panels (a) and (b) panels only one quarter of the domain is shown.)

With the thermal analogy, we can import results from the passive-scalar problem. Isichenko *et al.* (1989) and Gruzinov *et al.* (1990) discuss the effective diffusivity of a passive scalar due to advection by a steady monoscale streamfunction. Using a scaling argument, Isichenko *et al.* (1989) show that in the high Péclet number limit the effective diffusivity of a steady monoscale flow is  $D_{\text{eff}} = DP^{10/13}$ , where  $D$  is the small molecular diffusivity and  $P$  is the Péclet number; the exponent 10/13 relies on critical exponents determined by percolation theory. Applying Isichenko's passive-scalar results to the  $\beta = 0$  form-stress problem we obtain the scaling

$$\mu_{\text{eff}} = c \mu^{3/13} \eta_{\text{rms}}^{10/13}, \quad \text{and} \quad \frac{\mu \bar{U}}{F} = \frac{1}{c} \left( \frac{\mu}{\eta_{\text{rms}}} \right)^{10/13}, \quad (6.11)$$

where  $c$  is a dimensionless constant. Numerical solutions of (2.4) and (2.6) summarized in figure 16 confirm this remarkable “ten-thirteenths” scaling and show that the constant  $c$  in (6.11) is close to one. The dashed lines in figures 8 and 9 that correspond to the series with  $\beta \ell_\eta/\eta_{\text{rms}} \leqslant 0.1$  indicate the approximation (6.11) with  $c = 1$ .

To summarize: the weakly forced regime is divided into the easy large- $\beta$  case, in which  $\mu_{\text{eff}}$  in (6.4) applies, and the more difficult case with small or zero  $\beta$ . In the difficult case, with closed geostrophic contours, Isichenko's  $\beta = 0$  scaling law in (6.11) is the main analytic result. The value of  $\beta \ell_\eta/\eta_{\text{rms}}$  separating these two regimes in the

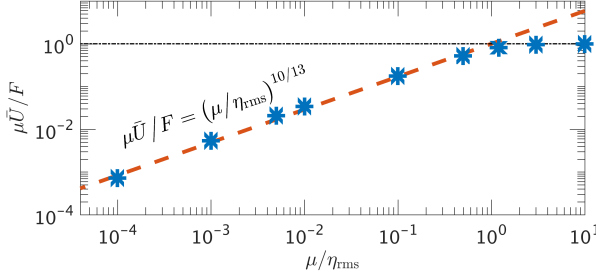


Figure 16: The large-scale flow for weakly forced solutions ( $F/(\mu\eta_{\text{rms}}\ell_\eta) = 10^{-3}$ ) with  $\beta = 0$  as a function of  $\mu/\eta_{\text{rms}}$ . The dashed line shows the prediction (6.11) for  $c = 1$ .

schematic of figure 14 is identified with the  $\beta$  below which (6.4) underestimates  $\mu U/F$  compared to (6.11). For the topography used in this work, and taking  $c = 1$  in (6.11), this is  $\beta\ell_\eta/\eta_{\text{rms}} = 0.17$ . (If we choose  $c = 0.5$  the critical value is  $\beta\ell_\eta/\eta_{\text{rms}} = 0.24$ .) This rationalizes why the  $\beta = 0$  result in (6.11) works better than  $\mu_{\text{eff}}$  in (6.4) for  $\beta\ell_\eta/\eta_{\text{rms}} < 0.35$ : see figure 9.

## 7. The strongly forced regime, $F/(\mu\eta_{\text{rms}}\ell_\eta) \gg 1$

We turn now to the upper branch, i.e., to the flow beyond the drag crisis. In this strongly forced regime the flow is steady:  $\psi' = U' = 0$  and the QL theory gives good results for all values of  $\beta\ell_\eta/\eta_{\text{rms}}$ .

Assuming that the large-scale flow is much greater than the phase speed of Rossby waves excited by the topography,  $U \gg \beta\ell_\eta^2$ , we can simplify the QL approximation to  $\langle \bar{\psi}\eta_x \rangle$  in (5.5) by neglecting all terms smaller than  $\beta\ell_\eta^2/U$ . Thus we obtain

$$\langle \psi\eta_x \rangle = \frac{\mu\eta_{\text{rms}}^2\ell_\eta^2}{U} + O(\beta\ell_\eta^2/U)^2. \quad (7.1)$$

This result is independent of  $\beta$  up to  $O(\beta\ell_\eta^2/U)^2$ . Using (7.1) in the large-scale zonal momentum equation (5.2), while keeping in mind that  $0 \leq U \leq F/\mu$ , we solve a quadratic equation for  $U$  to obtain:

$$\frac{\mu U}{F} = \frac{1}{2} + \sqrt{\frac{1}{4} - \left( \frac{\mu\eta_{\text{rms}}\ell_\eta}{F} \right)^2}. \quad (7.2)$$

The location of the drag crisis depends on  $\beta$ , and on details of the topography that are beyond the reach of the QL approximation. But once the solution is on the upper branch these complications are irrelevant e.g., (7.2) does not contain  $\beta$ . The dashed curve in figure 17 compares (7.2) to numerical solutions of the full system and shows close agreement.

We get further intuition about the structure of the upper-branch flow by simplifying the quasi-linear solution (5.3) in the limit  $U \rightarrow \infty$ . Neglecting all terms smaller than  $U^{-1}$ :

$$\psi = -\nabla^{-2}\eta - \frac{\mu}{U} \sum_{\mathbf{k}} \frac{\eta_{\mathbf{k}} e^{i\mathbf{k}\cdot\mathbf{x}}}{ik_x|\mathbf{k}|^2} + \frac{\beta}{U} \sum_{\mathbf{k}} \frac{\eta_{\mathbf{k}} e^{i\mathbf{k}\cdot\mathbf{x}}}{|\mathbf{k}|^4} + O(U^{-2}). \quad (7.3)$$

At leading order in (7.3),  $\zeta$  and  $\eta$  are completely anti-correlated so that  $q$  is of order  $U^{-1}$ . Figure 12(a) confirms that on the upper branch the correlation of  $\bar{\zeta}$  with  $\eta$  is close

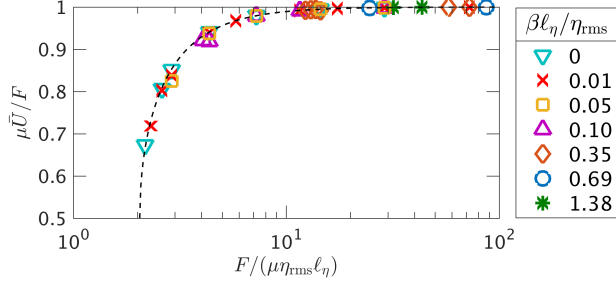


Figure 17: A detailed view of the upper-branch flow regime i.e., the upper-right part of figure 9(a), together with the analytic prediction (7.2) (dashed).

to  $-1$ . Only the second term on the right of (7.3) contributes to the form stress; this higher-order contribution produces the form stress in (7.1) for a monoscale topography.

## 8. Intermediate forcing: the eddy saturation regime and the drag crisis

In sections 6 and 7 we discussed limiting cases with small and large forcing respectively. In both these limits the solution is steady i.e., there are no transient eddies. We now turn to the more complicated situation with forcing of intermediate strength. In this regime the solution has transient eddies and numerical solution shows that these produce drag that is additional to the QL prediction (see figure 13 and related discussion). The eddy saturation regime, in which  $U$  is insensitive to large changes in  $F/(\mu\eta_{\text{rms}}\ell_\eta)$  (see figure 11), is also characterized by forcing of intermediate strength: the solution described in section 3.3 is an example. Thus a goal is to better understand the eddy saturation regime and its termination by the drag crisis.

### 8.1. Eddy saturation regime

As wind stress increases transient eddies emerge: in figure 10 this instability of the steady solution occurs very roughly at  $F/(\mu\eta_{\text{rms}}\ell_\eta) = 1.5 \times 10^{-2}$  for all values of  $\beta$ . The power integrals in appendix A show that the transient eddies gain kinetic energy from the standing eddies  $\bar{\psi}$  through the conversion term  $\langle \bar{\psi} \nabla \cdot \mathbf{E} \rangle$ , where

$$\mathbf{E} \stackrel{\text{def}}{=} \overline{\mathbf{U}' q'}, \quad (8.1)$$

is the time-averaged eddy PV flux. The conclusions from appendix A are summarized in figure 22 by showing the energy and enstrophy transfers among the four flow components  $\bar{U}$ ,  $U'$ ,  $\bar{\psi}$  and  $\psi'$ .

Figure 18 compares the numerical solutions of (2.4) and (2.6) with the prediction of the QL approximation (asterisks \* versus the solid curve) for the case with  $\beta\ell_\eta/\eta_{\text{rms}} = 1.38$ . The QL approximation has a stronger large-scale flow than that of the full system in (2.4) and (2.6). Moreover the full system is more impressively eddy saturated than the QL approximation. There are at least two causes for these failures of the QL approximation: (i) QL assumes steady flow and has no way of incorporating the effect of transient eddies on the time-mean flow and (ii) QL neglects the term  $J(\bar{\psi}, \bar{q})$ .

We address these points by following Rhines & Young (1982) and approximating the effect of the transient eddies as PV diffusion:

$$\nabla \cdot \mathbf{E} \approx -\kappa_{\text{eff}} \nabla^2 \bar{q}. \quad (8.2)$$

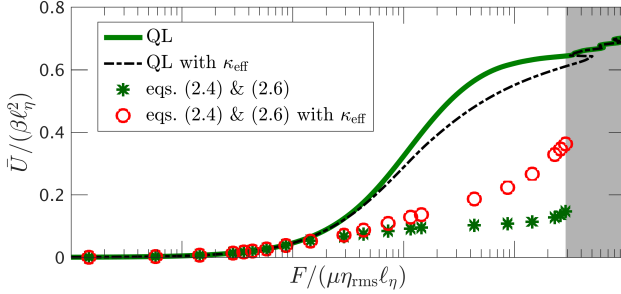


Figure 18: The eddy saturation regime for  $\beta\ell_\eta/\eta_{\text{rms}} = 1.38$ . Asterisks \* indicate numerical solutions of (2.4) and (2.6). Circles  $\circ$  show the numerical solutions of (2.4) and (2.6) with the added PV diffusion,  $\kappa_{\text{eff}} \nabla^2 q$ . The solid curve is the QL prediction (5.4) and the dashed-dot curve is the QL prediction with added PV diffusion. The shaded area marks regime beyond the drag crisis.

First, we test the approximation (8.2) by a brute-force computation of  $\mathbf{E}$  and visual comparison of the two fields. Figures 19(a) and (b) compare  $\nabla \cdot \mathbf{E}$  with  $-\nabla^2 \bar{q}$  for the case with  $\beta\ell_\eta/\eta_{\text{rms}} = 1.38$ , for wind stress  $F/(\mu\eta_{\text{rms}}\ell_\eta) = 26.09$  which is just before the drag crisis i.e., where the transient eddies are the most energetic. The two fields show visual agreement, implying that the PV diffusion approximation (8.2) might work. We choose  $\kappa_{\text{eff}}$  by substituting (8.2) into the transient eddy energy equation (A 4c). With this closure based of the energy power integral, the PV diffusivity is

$$\kappa_{\text{eff}} = -\frac{\langle \psi' D\zeta' \rangle + \overline{U'} \langle \psi' \eta_x \rangle}{\langle \bar{\zeta} \bar{q} \rangle}. \quad (8.3)$$

The PV diffusivity diagnosed from (8.3) is shown in figure 20(a) for the series with  $\beta\ell_\eta/\eta_{\text{rms}} = 1.38$ .

With  $\kappa_{\text{eff}}$  in hand, can revisit the QL theory and ask for its prediction when the term  $\kappa_{\text{eff}} \nabla^2 q$  is added on the right hand side of (5.1). This way we include the effect of the transients on the time-mean flow but do not include the effect of the term  $J(\bar{\psi}, \bar{q})$ . The QL prediction is only slightly improved — see the dash-dotted curve in figure 18.

To include also the effect of the term  $J(\bar{\psi}, \bar{q})$  we obtain solutions of (2.4) and (2.6) with added PV diffusion in (2.4) with  $\kappa_{\text{eff}}$  as in figure 20(a). We find that the strength of the transient eddies is dramatically reduced: see figure 20(b). Thus the approximation (8.2) with the PV diffusivity supplied by (8.3) is self-consistent in the sense that we do not both resolve and parameterize transient eddies. Moreover, the large-scale flow with parameterized transient eddies is in much closer agreement with  $\bar{U}$  from the solutions with transient eddies — see figure 18. This striking quantitative agreement as we vary  $F/(\mu\eta_{\text{rms}}\ell_\eta)$  shows that at least in the case with  $\beta\ell_\eta/\eta_{\text{rms}} = 1.38$  the transient eddies act as PV diffusion on the time-mean flow.

Thus we conclude, that in addition to  $\beta$ , the main physical mechanisms operating in the eddy saturation regime are PV diffusion via the transient eddies and the mean advection of mean PV i.e., the term  $J(\bar{\psi}, \bar{q})$ .

There are two remarkable aspects of this success. First, it is important to use  $\kappa_{\text{eff}} \nabla^2 (\bar{\zeta} + \eta)$  in (8.2); if one uses only  $\kappa_{\text{eff}} \nabla^2 \bar{\zeta}$  then the agreement in figure 18 is degraded. Second, PV diffusion does not decrease the amplitude of the standing eddies: see figure 20(c). Instead, PV diffusion increases the form stress  $\langle \bar{\psi} \eta_x \rangle$  by increasing the correlation of  $\psi$  with  $\eta_x$ .

Unfortunately, the success of the PV diffusion parameterization does not extend to

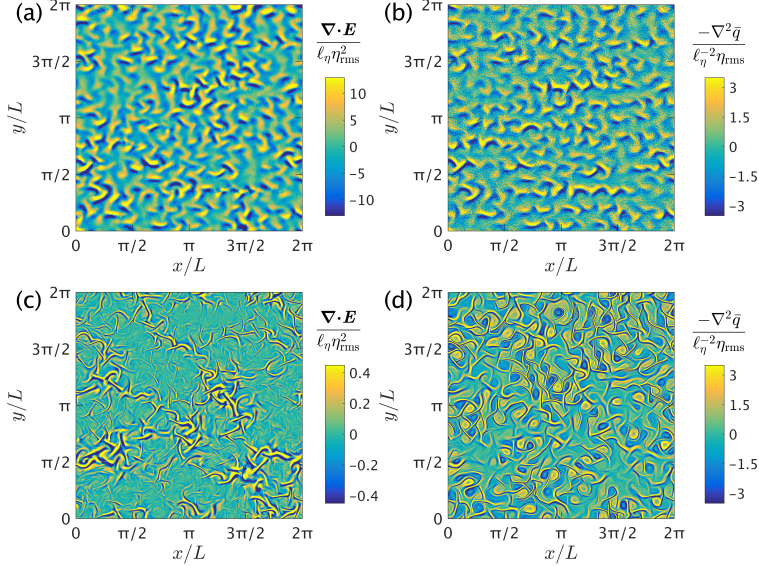


Figure 19: A comparison of the eddy flux divergence  $\nabla \cdot \mathbf{E}$  with  $-\nabla^2 \bar{q}$  for the examples from sections 3.2 and 3.3. The top row is the case  $\beta\ell_\eta/\eta_{\text{rms}} = 1.38$  with open geostrophic contours, shown in figures 5 and 6. The bottom row is the case  $\beta\ell_\eta/\eta_{\text{rms}} = 0.1$  with mainly closed geostrophic contours, shown in figures 3 and 4.

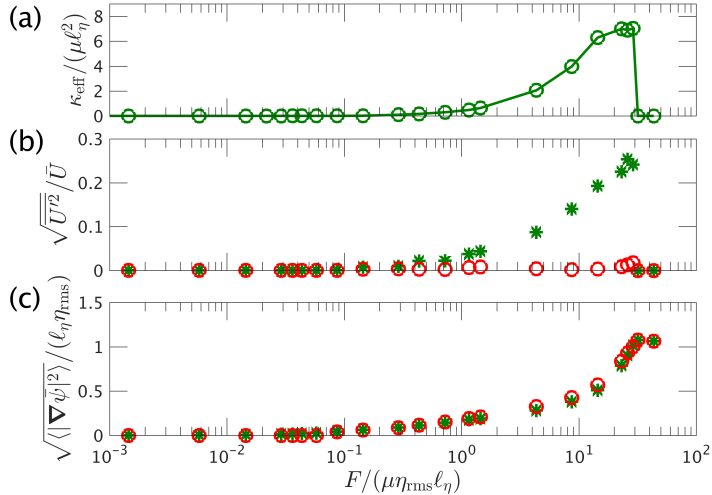


Figure 20: (a) The effective PV diffusivity,  $\kappa_{\text{eff}}$ , diagnosed from (8.3) for the series of solutions with  $\beta\ell_\eta/\eta_{\text{rms}} = 1.38$ . (b) The strength of the transient eddies for this series of solutions (asterisks \*) and for the solutions with parameterized transient eddies (circles o). (c) The r.m.s. velocity of the standing eddies,  $\sqrt{\langle|\nabla\psi|^2\rangle}$ , for the same solutions.

cases with small  $\beta\ell_\eta/\eta_{\text{rms}}$ , such as  $\beta\ell_\eta/\eta_{\text{rms}} = 0.10$ ; see figures 19(c) and (d). For small  $\beta\ell_\eta/\eta_{\text{rms}}$  the flow is strongly affected by the detailed structure of the topography. The solution described in section 3.2 shows that flow is channeled and a parametrization that does account the actual structure of the topography is, probably, doomed to fail. In fact, for  $\beta\ell_\eta/\eta_{\text{rms}} = 0.1$  the  $\kappa_{\text{eff}}$  diagnosed according to (8.3) is negative because  $\langle\bar{\zeta}\bar{q}\rangle < 0$ .

In conclusion, the PV diffusion approximation (8.2) gives good quantitative results if the flow does not crucially depend on the structure of the topography itself i.e., for large  $\beta\ell_\eta/\eta_{\text{rms}}$  so that the geometry is dominated by open geostrophic contours. In this regime the PV diffusion parameterization constitutes, to our best knowledge, a first theory for eddy saturation. However, for the quasi-realistic case of  $\beta\ell_\eta/\eta_{\text{rms}} = 0.1$  when the flow depends crucially on the geometric characteristics of the topography the  $\kappa_{\text{eff}}$ -theory does not apply.

### 8.2. Drag crisis

In this section we provide some further insight into the drag crisis. We argue that the requirement of enstrophy balance among the flow components leads to a transition from the lower to the upper branch. We make this argument by constructing lower bounds on the large-scale flow  $\bar{U}$  based on energy and enstrophy power integrals.

We consider a “test streamfunction” that is efficient at producing form stress:

$$\psi^{\text{test}} = \alpha\eta_x, \quad (8.4)$$

with the positive constant  $\alpha$  to be determined by satisfying either the energy or the enstrophy power integrals from appendix A. A maximum form stress corresponds to a minimum large-scale flow  $\bar{U}^{\min}$ , which is determined by substituting (8.4) into the time average of zonal momentum equation (2.6):

$$\mu\bar{U}^{\min} = F - \alpha\langle\eta_x^2\rangle. \quad (8.5)$$

We can determine  $\alpha$  so that the eddy energy power integral (A 4c)+(A 4d) is satisfied

$$0 = \bar{U}^{\min}\alpha\langle\eta_x^2\rangle - \mu\alpha^2\langle|\nabla\eta_x|^2\rangle - \nu\alpha^2\langle(\nabla^2\eta_x)^2\rangle. \quad (8.6)$$

The averages above are evaluated using properties of monoscale topography such as

$$\langle\eta_x^2\rangle = \frac{\eta_{\text{rms}}^2}{2\ell_\eta^2}, \quad \langle(\nabla^2\eta_x)^2\rangle = \frac{\eta_{\text{rms}}^2}{2\ell_\eta^6}. \quad (8.7)$$

Solving (8.5) and (8.6) for  $\alpha$  and  $\bar{U}^{\min}$  we obtain a lower bound on the large-scale flow based on the energy constraint

$$\bar{U} \geq \underbrace{\frac{F}{\mu} \left[ 1 + \frac{\eta_{\text{rms}}^2}{2(\mu + \nu/\ell_\eta^2)^2} \right]^{-1}}_{\stackrel{\text{def}}{=} \bar{U}_E^{\min}}. \quad (8.8)$$

Alternatively, one can determine  $\alpha$  and  $\bar{U}^{\min}$  by satisfying the eddy enstrophy power integral (A 6b)+(A 6c). This leads to a second bound

$$\bar{U} \geq \underbrace{\frac{F}{\mu} \left[ 1 - \frac{\beta\eta_{\text{rms}}^2\ell_\eta^2}{2(\mu + \nu/\ell_\eta^2)F} \right]}_{\stackrel{\text{def}}{=} \bar{U}_Q^{\min}}. \quad (8.9)$$

Thus

$$U \geq \max(\bar{U}_E^{\min}, \bar{U}_Q^{\min}). \quad (8.10)$$

The test function in (8.4) does not closely resemble the realized flow so the bound above is not tight. Nonetheless it does capture some qualitative properties of the turbulent solutions.

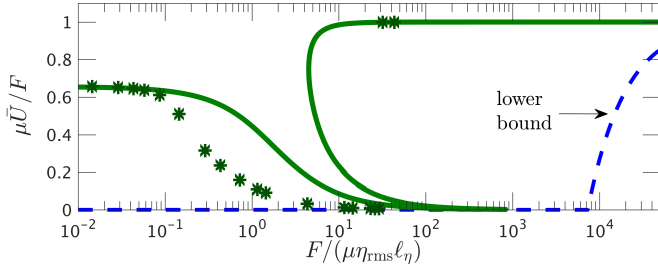


Figure 21: The numerical solutions of (2.4) and (2.6) (asterisks \*) and the QL prediction (5.4) (solid curve). The dashed line shows the lower bound (8.10).

(Using a more elaborate test function with two parameters one can satisfy both the energy and enstrophy power integrals simultaneously and obtain a single bound. However, the calculation is much longer and the result is not much better than the relatively simple (8.10).)

The lower bound (8.10) is shown in figure 21 for the case with  $\beta\ell_\eta/\eta_{\text{rms}} = 1.38$  together with the numerical solution of the full nonlinear equations (2.4) and (2.6) and the QL prediction. Although it cannot be clearly seen, the energy bound  $\bar{U}_E^{\min}$  does not allow  $\bar{U}$  to vanish completely, e.g. for the  $\mu/\eta_{\text{rms}} = 10^{-2}$  we have that  $\mu\bar{U}/F \geq 2 \times 10^{-4}$ . On the other hand, the dominance of the enstrophy bound  $\bar{U}_Q^{\min}$  at high forcing explains the occurrence of the drag crisis: the enstrophy power integral *requires* that the large-scale flow *must* transition from the lower to the upper branch as  $F$  is increased beyond a certain value.

These bounds provide a qualitative explanation for the existence the drag crisis. However, the critical forcing predicted by the enstrophy bound dominance overestimates the actual value of the drag crisis. For example, for the case with  $\beta\ell_\eta/\eta_{\text{rms}} = 1.38$ , shown in figure 21,  $\bar{U}_Q^{\min}$  becomes the lower bound at a value of  $F/(\mu\eta_{\text{rms}}\ell_\eta)$  that is about 240 times larger than the actual drag crisis point. We have no reason to expect these bounds to be tight: they do not depend on the actual structure of topography itself but only on gross statistical properties, e.g.  $\eta_{\text{rms}}$ ,  $\ell_\eta$ ,  $L_\eta$ . For example, a topographic PV of the form:

$$\eta = \sqrt{2}\eta_{\text{rms}} \cos(x/\ell_\eta), \quad (8.11)$$

has identical statistical properties to the monoscale topography and therefore imposes the same bounds. But with the topography in (8.11) there is a laminar solution with  $\psi_y = 0$  and, as a result, also  $J(\psi, q) = 0$ . In this case the QL solution (5.3) is an exact solution of the full nonlinear equations (2.4) and (2.6) and the bound (8.10) is tight.

## 9. Discussion and conclusion

Using a one-layer quasi-geostrophic model forced by a steady uniform zonal wind stress we have investigated the regimes of geostrophic turbulence resulting from the interaction of topography with large-scale currents.

In the limit that the domain is much larger than the topographic length-scale  $\ell_\eta$  the topography is “self-averaging”: results obtained with a single topography realization coincide with ensemble averages over different topography realizations (see figure 8 and surrounding discussion). This is important because oceanographers are likely to remain ignorant of small-scale topography of ocean floor (Sandwell *et al.* 2014) — be specific, is small scale 15km?. Thus topographic statistics obtained by detailed mapping of limited

representative sub-regions of the sea floor may be used to estimate topographic form stress over much larger regions.

In figure 9, as wind stress increases there is a transition among three flow regimes: (i) the weakly forced, linear regime in which the flow is steady and in which  $\mu U/F$  varies with  $\beta \ell_\eta / \eta_{\text{rms}}$ , (ii) an intermediate regime in which the flow develops transient eddies and in which most of the wind stress is balanced by form stress, and (iii) the strongly forced regime in which the flow is again steady with almost no topographic form stress and very large  $U$  (upper branch solution). The upper-branch flow in regime (iii) is independent of  $\beta \ell_\eta / \eta_{\text{rms}}$ . If  $\beta \ell_\eta / \eta_{\text{rms}} \neq 0$  the transition from the intermediate regime (ii) to the upper branch (iii) occurs as a discontinuous jump that has been previously identified in low-order modes (Charney & DeVore 1979).

The regimes (i) through (iii) summarized above are not quirks of the monoscale topography: using a multiscale topography with a  $k^{-2}$  power spectral density, we found similar qualitative behaviors (not shown).

Regarding the linear regime (i), if  $\beta \ell_\eta / \eta_{\text{rms}}$  is significantly less than one then most of the wind stress is balanced by form stress and  $U$  is much less than  $F/\mu$ . Note especially that this is the case for  $\beta = 0$ ; this shows that topographic form stress is not the same as wave drag associated with stationary Rossby waves. On the other hand, non-zero  $\beta$  is a necessary requirement for existence of the eddy saturation regime, which is also characterized by large topographic form stress. We summarize by saying that although  $\beta$  is not required for topographic form stress, it helps.

In the linear regime, with no transient eddies, the closed-streamline theorem of appendix B implies that there cannot be any recirculating flow i.e., there are no closed eddies. Instead, the flow is characterized by stagnant zones separated by boundary layers threading across the domain (figure 15). The closed-streamline theorem also rationalized the stagnant-zone structure of solutions with weak transient eddies (figure 4).

We have revisited Davey's (1980) QL theory (section 5), and discussed its validity in various parameter ranges (sections 6, 7 and 8). The QL theory gives asymptotic scaling laws provided that  $\beta$  is large enough to open the geostrophic contours. However, if the geostrophic contours are closed by topographic PV, the QL approximation fails. In this case we can invoke the useful thermal analogy of Welander (1968) and import results from percolation theory (Isichenko 1992) to derive the “ten-thirteenths” scaling law for the strength of the large-scale flow as a function of the forcing and drag coefficient (figure 16).

A surprising discovery is that the model has an eddy saturation regime. This is surprising because initially Straub (1993) had speculated that both baroclinicity and channel walls are necessary for eddy saturation, both of which are absent from the model. Referring to figure 11, eddy saturation occurs for  $\beta \ell_\eta / \eta_{\text{rms}} \geq 0.35$  i.e, when there is a significant fraction of open geostrophic contours (figure 2). In parameter regimes that exhibit eddy saturation we invariably find strong transient eddies. PV diffusion in (8.2) is a good parameterization for these transient eddies because (8.2): (i) removes the transients and results in a steady solution; (ii) does not affect the strength of the standing eddies; (iii) produces eddy saturation by increasing the correlation of  $\bar{\psi}$  with  $\eta_x$  (section 8.1).

The authors acknowledge comments and discussion with P. J. Ioannou, N. A. Bakas and T. D. Drivas. NCC was supported by the NOAA Climate & Global Change Postdoctoral Fellowship Program, administered by UCAR's Visiting Scientist Programs. WRY was supported by the National Science Foundation under OCE-1357047. The MATLAB code used in this paper is available at the github repository: [https://github.com/navidcy/QG\\_ACC\\_1layer](https://github.com/navidcy/QG_ACC_1layer).

## Appendix A. Energy and enstrophy balances

In this appendix we derive energy and enstrophy evolution as well as the time-averaged energy and enstrophy balances for each of the four flow components:  $\bar{U}$ ,  $U'$ ,  $\bar{\psi}$  and  $\psi'$ . Following (2.7), we represent all flow fields as a time-mean plus a transient; note that  $\bar{q} = \bar{\zeta} + \eta$  and  $q' = \zeta'$ . Equations (2.4) and (2.6) decompose into:

$$\mathbf{J}(\bar{\psi} - \bar{U}y, \bar{q} + \beta y) + \nabla \cdot \mathbf{E} + D\bar{\zeta} = 0, \quad (\text{A } 1a)$$

$$q'_t + \mathbf{J}(\psi' - U'y, \bar{q} + \beta y) + \mathbf{J}(\bar{\psi} - \bar{U}y, q') + \nabla \cdot (\mathbf{E}'' - \mathbf{E}) + D\zeta' = 0, \quad (\text{A } 1b)$$

$$F - \mu\bar{U} - \langle \bar{\psi}\eta_x \rangle = 0, \quad (\text{A } 1c)$$

$$U'_t = -\mu U' - \langle \psi'\eta_x \rangle, \quad (\text{A } 1d)$$

where the eddy PV fluxes are  $\mathbf{E}'' \stackrel{\text{def}}{=} \mathbf{U}'q'$  and  $\mathbf{E} \stackrel{\text{def}}{=} \overline{\mathbf{U}'q'}$ .

### A.1. Energy

Following the definitions in (2.9), the energy of each flow component is:

$$E_{\bar{U}} = \frac{1}{2}\bar{U}^2, \quad E_{U'} = \frac{1}{2}U'^2, \quad E_{\bar{\psi}} = \frac{1}{2}\langle |\nabla\bar{\psi}|^2 \rangle \quad \text{and} \quad E_{\psi'} = \frac{1}{2}\langle |\nabla\psi'|^2 \rangle. \quad (\text{A } 2)$$

Thus, the total energy of the large-scale flow and of the eddies is:

$$E_U = E_{\bar{U}} + E_{U'} + \bar{U}U' \quad \text{and} \quad E_{\psi} = E_{\bar{\psi}} + E_{\psi'} + \langle \nabla\bar{\psi} \cdot \nabla\psi' \rangle. \quad (\text{A } 3)$$

The cross-terms above are removed by time-averaging.

To obtain a power integral for the transient large-scale energy we multiply (A 1d) by  $U'$  and time average

$$\overline{E_{U'}} : \quad 0 = -\mu\overline{U'^2} - \overline{U'}\langle \psi'\eta_x \rangle. \quad (\text{A } 4a)$$

The time-mean large-scale flow energy balance is obtained by multiplying (A 1c) by  $\bar{U}$

$$\overline{E_{\bar{U}}} : \quad 0 = F\bar{U} - \mu\bar{U}^2 - \bar{U}\langle \bar{\psi}\eta_x \rangle. \quad (\text{A } 4b)$$

Summing (A 4a) and (A 4b) we obtain the energy power integral for the total (standing plus transient) large-scale flow.

To obtain an energy power integral for the transient eddies, we multiply (A 1a) by  $-\psi'$ , average over the domain and time average

$$\overline{E_{\psi'}} : \quad 0 = \overline{U'}\langle \psi'\eta_x \rangle - \langle \bar{\psi}\nabla \cdot \mathbf{E} \rangle + \langle \psi'D\bar{\zeta} \rangle. \quad (\text{A } 4c)$$

The energy power integral for the standing eddies is obtained by multiplying (A 1a) with  $-\bar{\psi}$  and averaging over the domain

$$\overline{E_{\bar{\psi}}} : \quad 0 = \bar{U}\langle \bar{\psi}\eta_x \rangle + \langle \bar{\psi}\nabla \cdot \mathbf{E} \rangle + \langle \bar{\psi}D\bar{\zeta} \rangle. \quad (\text{A } 4d)$$

Summing (A 4c) and (A 4d) the conversion term  $\langle \bar{\psi}\nabla \cdot \mathbf{E} \rangle$  cancels and we obtain the energy power integral (2.11) for the total (standing plus transient) eddy field.

The time mean of the energy integral in (2.10a) is the sum of equations (A 4). Note that from (A 4a) we have that  $\overline{U'}\langle \psi'\eta_x \rangle < 0$  and thus from (A 4c) we infer that  $\langle \bar{\psi}\nabla \cdot \mathbf{E} \rangle < 0$ . The energy power integrals (A 4) are summarized in figure 22(a).

### A.2. Enstrophy

The enstrophy of each flow component is:

$$Q_{\bar{U}} = \beta\bar{U}, \quad Q_{U'} = \beta U', \quad Q_{\bar{\psi}} = \frac{1}{2}\langle \bar{q}^2 \rangle \quad \text{and} \quad Q_{\psi'} = \frac{1}{2}\langle q'^2 \rangle, \quad (\text{A } 5)$$

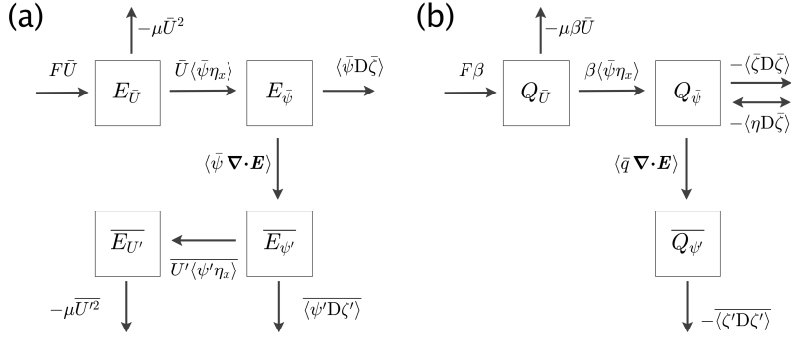


Figure 22: The energy and enstrophy transfers between the four flow components: time-mean large-scale flow  $\bar{U}$ , standing eddies  $\bar{\psi}$ , and the corresponding transient components  $U'$  and  $\psi'$ .

The transient large-scale flow has by definition  $\overline{Q_{U'}} = 0$ . The enstrophy power integrals follow by manipulations similar to those in Appendix A.1

$$Q_{\bar{U}} : \quad 0 = F\beta - \mu\beta\bar{U} - \beta\langle\bar{\psi}\eta_x\rangle, \quad (\text{A } 6a)$$

$$Q_{\bar{\psi}} : \quad 0 = \beta\langle\bar{\psi}\eta_x\rangle - \langle\bar{q}\nabla\cdot E\rangle - \langle\bar{\zeta}D\bar{\zeta}\rangle - \langle\eta D\bar{\zeta}\rangle, \quad (\text{A } 6b)$$

$$\overline{Q_{\psi'}} : \quad 0 = \langle\bar{q}\nabla\cdot E\rangle - \langle\zeta'D\zeta'\rangle. \quad (\text{A } 6c)$$

The time mean of the enstrophy integral in (2.10b) is the sum of equations (A 6). Equation (A 6c) implies that  $\langle\bar{q}\nabla\cdot E\rangle > 0$ ; the term  $\langle\eta D\bar{\zeta}\rangle$  in (A 6b) can have either sign. The enstrophy power integrals (A 6) are summarized in figure 22(b).

## Appendix B. A closed-streamline theorem

Using the decomposition into standing and transient eddies in (2.7) the time-mean QGPV equation for  $D = \mu$  is

$$J(\Psi, \bar{q} + \beta y) + \nabla \cdot E = -\mu \nabla^2 \Psi, \quad (\text{B } 1)$$

where  $\Psi \stackrel{\text{def}}{=} \bar{\psi} - \bar{U}y$ .

Modifying arguments first made by [Batchelor \(1956\)](#), we integrate (B 1) over the area within a closed curve  $\mathcal{C}$  on which  $\Psi$  is constant. The integral of  $J(\Psi, \bar{q} + \beta y)$  over such an area is zero so that

$$\oint (\mathbf{E} + \mu \nabla \Psi) \cdot \mathbf{n}_{\mathcal{C}} d\ell_{\mathcal{C}} = 0. \quad (\text{B } 2)$$

In (B 2),  $d\ell_{\mathcal{C}}$  is the arclength around the closed curve  $\mathcal{C}$  and  $\mathbf{n}_{\mathcal{C}}$  is the outward unit normal to  $\mathcal{C}$ .

We now show that if there are no transient eddies,  $\mathbf{E} = 0$ , then  $\nabla \Psi = 0$  on  $\mathcal{C}$ . Suppose to the contrary that  $\nabla \Psi \neq 0$  on  $\mathcal{C}$ . Then  $\mathcal{C}$  is a closed time-mean streamline with unit normal  $\mathbf{n}_{\mathcal{C}} = \pm \nabla \Psi / |\nabla \Psi|$ , where plus sign applies if  $\mathcal{C}$  encloses a low and the minus if the streamline encloses a high. Thus (B 2) reduces to

$$\mu \oint |\nabla \Psi| d\ell_{\mathcal{C}} = 0, \quad (\text{B } 3)$$

implying that  $|\nabla \Psi| = 0$  on  $\mathcal{C}$  violating the initial premise. Therefore,  $\nabla \Psi = 0$  on  $\mathcal{C}$ .

We conclude that  $\nabla\Psi$  is non-zero only on curves that do not close within the domain i.e., curves which span the domain, such as the  $\eta = 0$  contour in figure 15(a) and (b). In figure 15 the forcing is weak so that there are no transient eddies and the flat terraces are almost totally stagnant regions with  $|\nabla\Psi| = 0$ . The terraces are separated by cliffs: these boundary layers correspond to open streamlines threading through the domain by following the  $\eta = 0$  contour.

The situation is less clear-cut for the more strongly forced solution in figure 4: this flow has transient eddies,  $\mathbf{E} \neq 0$ , and therefore (B2) is not dispositive. Nonetheless the transient eddies are sufficiently weak so that bumpy terraces, with only small variations in  $\Psi$ , are still evident in figure 4.

## Appendix C. Form stress for isotropic topography

For the case of isotropic topography analytic progress follows to the QL expression for the form stress by converting the sum over  $\mathbf{k}$  in (5.4) into an integral:

$$\langle\psi\eta_x\rangle = U \int \frac{\mu k_x^2 |\mathbf{k}|^2 |\hat{\eta}(\mathbf{k})|^2}{\mu^2 |\mathbf{k}|^4 + k_x^2 (\beta - |\mathbf{k}|^2 U)^2} d^2\mathbf{k}, \quad (\text{C } 1)$$

where  $\hat{\eta}(\mathbf{k}) \stackrel{\text{def}}{=} \int \eta(\mathbf{x}) e^{-i\mathbf{k}\cdot\mathbf{x}} d^2\mathbf{x}$ . Now assume that the topography is isotropic, i.e. its power spectral density  $S(k)$  is only a function of the total wavenumber  $k \stackrel{\text{def}}{=} |\mathbf{k}|$  and defined as  $S(k) \stackrel{\text{def}}{=} 2\pi k |\hat{\eta}(\mathbf{k})|^2$ , so that  $\langle\eta^2\rangle = \int S(k) dk$ . In this case we further simplify the integral (C1) using polar coordinates  $(k_x, k_y) = k(\cos\theta, \sin\theta)$ :

$$\langle\psi\eta_x\rangle = \frac{U}{2\pi\mu} \int_0^\infty S(k) \oint \frac{\cos^2\theta}{1 + \xi \cos^2\theta} d\theta dk, \quad (\text{C } 2)$$

where  $\xi \stackrel{\text{def}}{=} (\beta - k^2 U)^2 / (\mu k)^2 > 0$ . The  $\theta$ -integral above is evaluated analytically so that

$$\langle\psi\eta_x\rangle = \mu U \int_0^\infty \frac{k^2 S(k) dk}{\mu^2 k^2 + (\beta - k^2 U)^2 + \mu k \sqrt{\mu^2 k^2 + (\beta - k^2 U)^2}}. \quad (\text{C } 3)$$

A special case for which the  $k$ -integral in (C3) can be evaluated in closed form is idealized monoscale topography:

$$S(k) = \eta_{\text{rms}}^2 \delta(k - \ell_\eta^{-1}). \quad (\text{C } 4)$$

Using (C4) the form stress in (C3) reduces to (5.5).

## REFERENCES

- ARBIC, B. K. & FLIERL, G. R. 2004 Baroclinically unstable geostrophic turbulence in the limits of strong and weak bottom Ekman friction: Application to midocean eddies. *J. Phys. Oceanogr.* **34** (10), 2257–2273.
- BATCHELOR, G. K. 1956 On steady laminar flow with closed streamlines at large Reynolds number. *J. Fluid Mech.* **1**, 177–190.
- BÖNING, C. W., DISPERT, A., VISBECK, M., RINTOUL, S. R. & SCHWARZKOPF, F. U. 2008 The response of the Antarctic Circumpolar Current to recent climate change. *Nat. Geosci.* **1** (1), 864–869.
- BRETHERTON, F. P. & HAIDVOGEL, D. B. 1976 Two-dimensional turbulence above topography. *J. Fluid Mech.* **78**, 129–154.
- BRETHERTON, F. P. & KARWEIT, M. 1975 Mid-ocean mesoscale modeling. In *Numerical models of ocean circulation*, pp. 237–249.

- CARNEVALE, G. F. & FREDERIKSEN, J. S. 1987 Nonlinear stability and statistical mechanics of flow over topography. *J. Fluid Mech.* **175**, 157–181.
- CHARNEY, J. G. & DEVORE, J. G. 1979 Multiple flow equilibria in the atmosphere and blocking. *J. Atmos. Sci.* **36**, 1205–1216.
- CHARNEY, J. G., SHUKLA, J. & MO, K. C. 1981 Comparison of a barotropic blocking theory with observation. *J. Atmos. Sci.* **38** (4), 762–779.
- COX, S. M. & MATTHEWS, P. C. 2002 Exponential time differencing for stiff systems. *J. Comput. Phys.* **176** (2), 430–455.
- DAVEY, M. K. 1980 A quasi-linear theory for rotating flow over topography. Part 1. Steady  $\beta$ -plane channel. *J. Fluid Mech.* **99** (02), 267–292.
- DONOHUE, K. A., TRACEY, K. L., WATTS, D. R., CHIDICHIMO, M. P. & CHERESKIN, T. K. 2016 Mean Antarctic Circumpolar Current transport measured in Drake Passage. *Geophys. Res. Lett.* **43**.
- EFROS, A. L. 1987 *Physics and Geometry of Disorder: Percolation Theory*. Imported Pubn.
- FARNETI, R., DOWNES, S. M., GRIFFIES, S. M., MARSLAND, S. J., BEHRENS, E., BENTSEN, M., BI, D., BIASTOCH, A., BÖNING, C., BOZEC, A., CANUTO, V. M., CHASSIGNET, E., DANABASOGLU, G., DANILOV, S., DIANSKY, N., DRANGE, H., FOGLI, P. G., GUSEV, A., HALLBERG, R. W., HOWARD, A., ILCIĆ, M., JUNG, T., KELLEY, M., LARGE, W. G., LEBOISSETIER, A., LONG, M., LU, J., MASINA, S., MISHRA, A., A., NAVARRA, NURSER, A. J. G., PATARA, L., SAMUELS, B. L., SIDORENKO, D., TSUJINO, H., UOTILA, P., WANG, Q. & YEAGER, S. G. 2015 An assessment of Antarctic Circumpolar Current and Southern Ocean meridional overturning circulation during 1958–2007 in a suite of interannual CORE-II simulations. *Ocean Model.* **93**, 84–120.
- FIRING, Y. L., CHERESKIN, T. K. & MAZLOFF, M. R. 2011 Vertical structure and transport of the Antarctic Circumpolar Current in Drake Passage from direct velocity observations. *J. Geophys. Res.-Oceans* **116** (C8), C08015.
- GOFF, J. A. 2010 Global prediction of abyssal hill root-mean-square heights from small-scale altimetric gravity variability. *J. Geophys. Res.* **115** (B12), B12104–16.
- GRUZINOV, A. V., ISICHENKO, M. B. & KALDA, YA. L. 1990 Two-dimensional turbulent diffusion. *Zh. Eksp. Teor. Fiz.* **97**, 476, [Sov. Phys. JETP, **70**, 263 (1990)].
- HAIDVOGEL, D. B. & BRINK, K. H. 1986 Mean currents driven by topographic drag over the continental shelf and slope. *J. Phys. Oceanogr.* **16**, 2159–2171.
- HART, J. E. 1979 Barotropic quasi-geostrophic flow over anisotropic mountains. *J. Atmos. Sci.* **36** (9), 1736–1746.
- HERRING, J. R. 1977 On the statistical theory of two-dimensional topographic turbulence. *J. Atmos. Sci.* **34** (11), 1731–1750.
- HOGG, A. MCC., MEREDITH, M. P., CHAMBERS, D. P., ABRAHAMSEN, E. P., HUGHES, C. W. & MORRISON, A. K. 2015 Recent trends in the southern ocean eddy field recent trends in the southern ocean eddy field. *J. Geophys. Res.-Oceans* **120**, 1–11.
- HOLLOWAY, G. 1987 Systematic forcing of large-scale geophysical flows by eddy-topography interaction. *J. Fluid Mech.* **184**, 463–476.
- HOLLOWAY, G. 1992 Representing topographic stress for large-scale ocean models. *J. Phys. Oceanogr.* **22** (9), 1033–1046.
- ISICHENKO, M. B. 1992 Percolation, statistical topography, and transport in random media. *Reviews of Modern Physics* **64** (4), 961–1043.
- ISICHENKO, M. B., KALDA, YA. L., TATARINOVA, E. B., TEL'KOVSKAYA, O. V. & YAN'KOV, V. V. 1989 Diffusion in a medium with vortex flow. *Zh. Eksp. Teor. Fiz.* **96**, 913–925, [Sov. Phys. JETP, **69**, 3 (1989)].
- KÄLLÉN, E. 1982 Bifurcation properties of quasigeostrophic, barotropic models and their relation to atmospheric blocking. *Tellus* **34** (3), 255–265.
- KASSAM, A.-K. & TREFETHEN, L. N. 2005 Fourth-order time-stepping for stiff PDEs. *SIAM J. Sci. Comput.* **26** (4), 1214–1233.
- KOENIG, Z., PROVOST, C., PARK, Y.-H., FERRARI, R. & SENNÉCHAEL, N. 2016 Anatomy of the Antarctic Circumpolar Current volume transports through Drake Passage. *J. Geophys. Res.-Oceans* **121** (4), 2572–2595.
- LEGRAS, B. & GHIL, M. 1985 Persistent anomalies, blocking and variations in atmospheric predictability. *J. Atmos. Sci.* **42**, 433–471.

- MARSHALL, G. J. 2003 Trends in the Southern Annular Mode from observations and reanalyses. *J. Climate* **16**, 4134–4143.
- MUNK, W. H. & PALMÉN, E. 1951 Note on the dynamics of the Antarctic Circumpolar Current. *Tellus* **3**, 53–55.
- PEDLOSKY, J. 1981 Resonant topographic waves in barotropic and baroclinic flows. *J. Atmos. Sci.* **38** (12), 2626–2641.
- RAMBALDI, S. & FLIERL, G. R. 1984 Form drag instability and multiple equilibria in the barotropic case. *Il Nuovo Cimento C* **6** (5), 505–522.
- RAMBALDI, S. & MO, K. C. 1984 Forced stationary solutions in a barotropic channel: Multiple equilibria and theory of nonlinear resonance. *J. Atmos. Sci.* **41** (21), 3135–3146.
- RHINES, P. B. & YOUNG, W. R. 1982 Homogenization of potential vorticity in planetary gyres. *J. Fluid Mech.* **122**, 347–367.
- SALMON, R., HOLLOWAY, G. & HENDERSHOTT, M. C. 1976 The equilibrium statistical mechanics of simple quasi-geostrophic models. *J. Fluid Mech.* **75** (4), 691–703.
- SANDWELL, D. T., MÜLLER, R. D., SMITH, W. H. F., GARCIA, E & FRANCIS, R. 2014 New global marine gravity model from CryoSat-2 and Jason-1 reveals buried tectonic structure. *Science* **346** (6205), 65–67.
- STRAUB, D. N. 1993 On the transport and angular momentum balance of channel models of the Antarctic Circumpolar Current. *J. Phys. Oceanogr.* **23**, 776–782.
- SWART, N. C. & FYFE, J. C. 2012 Observed and simulated changes in the Southern Hemisphere surface westerly windstress. *Geophys. Res. Lett.* **39** (16), L16711.
- TUNG, K.-K. & ROSENTHAL, A. J. 1985 Theories of multiple equilibria – A critical reexamination. Part I: Barotropic models. *J. Atmos. Sci.* **42**, 2804–2819.
- VENAILLE, A. 2012 Bottom-trapped currents as statistical equilibrium states above topographic anomalies. *J. Fluid Mech.* **699**, 500–510.
- WELANDER, P. 1968 Wind-driven circulation in one-and two-layer oceans of variable depth. *Tellus* **20** (1), 1–16.
- YODEN, S. 1985 Bifurcation properties of a quasi-geostrophic, barotropic, low-order model with topography. *J. Meteor. Soc. Japan* **63** (4), 535–546.
- ZOU, J. & HOLLOWAY, G. 1993 Forced-dissipated statistical equilibrium of large scale quasi-geostrophic flows over random topography. *Geophys. Astrophys. Fluid Dyn.* **69**, 55–75.